

TESSILATOR: a one-stop shop for measuring TESS rotation periods

A. S. Binks^{1,2*} & H. M. Günther¹

¹MIT Kavli Institute for Astrophysics and Space Research, Massachusetts Institute of Technology, Cambridge, MA 02139, USA

²Institut für Astronomie und Astrophysik, Eberhard-Karls Universität Tübingen, Sand 1, 72076 Tübingen, Germany

Accepted XXX. Received YYY; in original form ZZZ

ABSTRACT

We present a software package designed to produce photometric lightcurves and measure rotation periods from full-frame images taken by the Transiting Exoplanet Survey Satellite (TESS), which we name “TESSILATOR”. TESSILATOR is the only publicly-available code that will run a full lightcurve and rotation period (P_{rot}) analysis based on just a (list of) target identifier(s) or sky position(s) via a simple command-line prompt. This paper sets out to introduce the rationale for developing TESSILATOR, and then describes the methods, considerations and assumptions for: extracting photometry; dealing with potential contamination; accounting for natural and instrumental systematic effects; lightcurve normalisation and detrending; removing outliers and unreliable data; and finally, measuring the P_{rot} value and several periodogram attributes. Our methods have been tuned specifically to optimise TESS lightcurves and are independent from the pipelines developed by the TESS Science Processing Operations Center, meaning TESSILATOR can, in principle, analyse *any* target across the entire celestial sphere.

We compare TESSILATOR P_{rot} measurements with TESS-SPOC-derived lightcurves of 1,560 (mainly FGKM-type) stars across four benchmark open clusters (Pisces–Eridanus, the Pleiades, the Hyades and Praesepe) and a sample of nearby field M-dwarfs. From a vetted subsample of 864 targets we find an excellent return of P_{rot} matches for the first 3 open clusters (> 85 per cent) and a moderate (~ 60 per cent) match for the 700 Myr Praesepe and MEarth sample, which validates TESSILATOR as a tool for measuring P_{rot} . The TESSILATOR code is available at <https://github.com/alexibinks/tessilator>.

Key words: stars: rotation – surveys

1 INTRODUCTION

All stars (and celestial objects) rotate. The rate at which stars spin is governed by the angular momentum transfer processes that occur as mass density profiles and energy content are redistributed as they evolve. The time taken for a star to complete one full revolution on its rotational axis, commonly referred to as the rotation period (P_{rot}), is an age and mass-dependent quantity that is vital to determine the stellar radius and rotational velocity. Rotation is therefore a crucial feature that must be correctly accounted for in evolutionary models. Our lack of understanding of stellar rotation at young ages may be partially responsible for the large discrepancies amongst various models in terms of their age and mass calculations of pre-main sequence (PMS, 5 – 100 Myr) low-mass (spectral types FGK and M) stars (Bell et al. 2015; Binks et al. 2022). Whilst rotation has been known for decades to scale with other features of PMS evolution, such as magnetic activity (Skumanich 1972; Noyes et al. 1984; Mamajek & Hillenbrand 2008; Basri 2021) and Lithium depletion (Soderblom et al. 1993; Jeffries et al. 2021), a full picture of the effects that rotation has on these process is yet to emerge. Additional gaps in our understanding have been exposed at older ages, where stars of similar spectral-type are observed to spin-down slower than standard predictions (Curtis et al. 2019; Spada & Lanzafame 2020).

Whilst a magnetic wind-breaking model has been effective in partially reconciling the discrepancy (van Saders et al. 2016), the exact physical process that drive the wind-breaking are poorly understood.

Rapid rotation can act as an important indicator of stellar youth for solar-type and low-mass stars, where alternative age-dating methods may be less effective (Binks et al. 2015). By measuring P_{rot} and analysing photometric lightcurves, features or properties that are often difficult to detect, such as magnetic activity, flares, (unresolved) multiplicity and age can be placed on a quantitative basis. Models incorporating the evolution of stellar angular momentum (Schatzman 1962; Kraft 1967; Kawaler 1988; Zahn 1992; Gallet & Bouvier 2013; Garraffo et al. 2018; Amard et al. 2019) predict three main phases of spin evolution before they slowly brake in a quasi-static fashion upon reaching the zero-age main sequence (ZAMS). Stars are born with an initial P_{rot} , which is thought to be largely regulated at early ages through the locking of magnetospheric accretion funnels to their protoplanetary disks (Koenigl 1991; Bouvier 2007). Subsequent to disk dissipation (typically after ~ 10 Myr, through accretion processes and/or UV photoionisation, Gorti & Hollenbach 2009; Owen et al. 2011; Picogna et al. 2019) they spin up during PMS contraction. The peak angular velocity and time at which this occurs is mostly mass dependent, where low-mass stars tend to rotate faster, but take longer to spin up. Once Solar-type stars arrive on the ZAMS, angular momentum is gradually lost through mass-loss in stellar winds (Kraft 1967; Skumanich 1972), whereas low-mass

* E-mail: binks@astro.uni-tuebingen.de (ASB)

stars converge onto the slow-rotating sequence slower and they stay fast-rotating longer (Barnes 2003).

Efforts to characterise the distribution of P_{rot} amongst members in many star clusters spanning ages from the early PMS to a few Gyr have verified model predictions to some extent, and provided parameterised empirical models connecting P_{rot} , photometric colour and age. This framework, known as ‘‘Gyrochronology’’ (Barnes 2003, 2007; Angus et al. 2015, 2019), has the power not only to offer potentially precise ages for clusters (less so for individual stars), but acts as a rigorous test for angular momentum models. There are unilateral findings that P_{rot} scales with: the inverse of X-ray luminosity (Pallavicini et al. 1981) – a proxy for coronal activity; $\log R'_{HK}$ or the Ca II triplet – a proxy for chromospheric activity (Wilson 1978; Linsky et al. 1979; Suárez Mascareño et al. 2018; Toledo-Padrón et al. 2019); and the occurrence rate of stellar flares (Davenport 2016; Günther et al. 2020; Raetz et al. 2020).

Up until the early 2000s, the yields of P_{rot} measurements from most surveys were typically on the order of several tens or hundreds, and usually focused on particular regions of sky (e.g., star clusters, OB associations, moving groups). The acquisition of photometric lightcurves can be time consuming, requiring high-cadence time-series data, with observing baselines often lasting months. Whilst spectroscopic rotational velocity ($v \sin i$) measurements were more relatively abundant (Glebocki et al. 2000; De Medeiros et al. 2014), the ambiguity of their inclination angles can only provide lower-limits on inferred P_{rot} values. In the past two decades, the number of P_{rot} measurements swelled by several orders of magnitude, partially from dedicated surveys of open clusters (e.g., the MONITOR project, Irwin et al. 2007, 2008), but mostly from the analysis of vast quantities of stellar lightcurves from missions whose primary goals focused on detecting exoplanet transits. These include ground-based missions such the Hungarian Automated Telescope (HATNet, Bakos et al. 2002) and the Super-Wide Angle Search for Planets (SuperWASP, Pollacco et al. 2006) and satellite surveys such as the Co-Rotating Telescope (CoRoT, Auvergne et al. 2009), the latter of which was a pre-cursor to the ground-breaking Kepler (and subsequent K2) (Howell et al. 2014; Borucki 2016) and the Transiting Exoplanet Survey Satellite (TESS, Ricker et al. 2015) missions. This paper focuses on data obtained exclusively from TESS¹.

Launched in 2018 (and still acquiring data), TESS has so far identified in excess of 5 000 planets, and another $\sim 7\,000$ are predicted to be discovered (Kunimoto et al. 2022). It has collected time-series data for over 95 per cent of the sky at least once (with most regions having ≥ 2 scans) and should be virtually all-sky by late-2024. TESS provides data in two modes during each of its ~ 27 day observing sectors: firstly the 2-minute cadence lightcurves generated by the TESS Science Processing Operations Center (Jenkins et al. 2016; Caldwell et al. 2020) specialised for $\sim 2 \times 10^5$ stars selected as prime candidate exoplanet hosts, and secondly the longer cadence full frame image calibrations (FFICs) recorded across the whole detector in the 4 CCDs across 4 cameras that cover a $24^\circ \times 96^\circ$ sky segment. The latter of these TESS modes provides an unprecedented unique opportunity to acquire lightcurves for stars across the full celestial sphere.

Many methods have been developed to measure stellar P_{rot} , such as the generalised Lomb-Scargle periodogram (LSP, Lomb 1976; Scargle 1982; Zechmeister & Kürster 2009; VanderPlas 2018), Autocorrelation Function (ACF, McQuillan et al. 2013; Holcomb et al.

2022), Wavelet Transforms (WTs, Carter & Winn 2009; García et al. 2014; Claytor et al. 2022), Gaussian Processes (GPs, Angus et al. 2018; Aigrain & Foreman-Mackey 2023) or a mixture of these (Ceillier et al. 2017; Santos et al. 2019; Reinhold & Hekker 2020; Colman et al. 2024). Each of the methods have strengths and weaknesses. For the purpose of this work, we focus only on the LSP method.

Given the potential for TESS to provide P_{rot} values for an enormous number of stars, and the impact they could have on improving our understanding of stellar rotational evolution, we have developed a software package named ‘‘TESSILATOR’’. It is specifically designed as an all-in-one program which, for any given target (or list of targets) will: automatically download the TESS data; quantify contamination from neighbouring sources; perform aperture photometry and generate lightcurves; normalise, detrend and clean lightcurves; correct for general systematic features (if required); perform a LSP analysis to measure the P_{rot} and several parameters to assess the quality and reliability of the measurements, and evaluate a final P_{rot} for targets with multiple TESS sectors. In this paper we present TESSILATOR to the community. We provide a detailed description of TESSILATOR’s functions, the lightcurve and periodogram analysis and test the performance of the code by comparing P_{rot} measurements for a set of open clusters and nearby M-dwarf field stars.

In §2 we briefly outline the rationale for developing bespoke software for analysing TESS lightcurves. In §3 we describe how TESSILATOR performs each step described in the previous paragraph, and the underlying assumptions and considerations that lead to a processed lightcurve and P_{rot} measurement. To show how the TESSILATOR performs in practice, in §4 we compare TESSILATOR P_{rot} measurements for 1560 stars with results from a recent publication and also a large sample of field stars from several recently published variability surveys. We provide our conclusions and plans for future TESSILATOR projects in §5.

2 SOFTWARE FOR ANALYSING TESS DATA

The primary objective of TESSILATOR is to: perform aperture photometry for TESS image data; apply cleaning and detrending procedures to improve lightcurves; measure the P_{rot} using LSP analysis; and assess the quality and reliability of these results by accounting for the background contamination and various properties of the lightcurve and periodogram output. All this can be done with a single command line prompt, where the user is required only to provide the target name, or a text file containing a list of target names (or sky-positions, see §3.1.1).

2.1 Pre-existing TESS-based public codes

Whilst many software tools have been developed for analysing TESS lightcurves from FFIC data, here we simply highlight some of the most frequently used software packages and discuss their relative merits. Two of the most commonly cited TESS codes are ‘‘eleanor’’² (Feinstein et al. 2019) and ‘‘Lightkurve’’³ (Lightkurve Collaboration et al. 2018). Whilst both these pipelines perform a careful lightcurve extraction by correcting for the instrument systematics apriori and applying sophisticated point-spread function (PSF) photometry, the former is optimised for planet searches (in line with the main aim of the TESS mission) and does not measure P_{rot} and the latter, whilst

¹ A set of targets with Kepler K2 P_{rot} measurements is used in §4.1 as a comparative sample.

² <https://adina.feinste.in/eleanor/>

³ <https://docs.lightkurve.org/index.html>

offering a periodogram function to measure P_{rot} , does not provide any quality or reliability metrics for the lightcurve or periodogram. Neither of these tools provide means to measure P_{rot} directly from receiving simply a target as input, requiring the user to incorporate functions into their own code. Moreover, neither of these codes account for the effects of neighbouring sources which can strongly contaminate the measured flux for a given target. A similar code, TESSEXTRACTOR⁴ (Serna et al. 2021) is also available, but uses different methods to measure P_{rot} and does not provide a detailed output of the lightcurve vetting and periodogram results.

Two additional TESS codes have been recently published. The first one, developed by Rampalli et al. (2023, herein, R23), use TESS lightcurves that have been pre-vetted by TESS-SPOC and directly perform LSP to obtain P_{rot} . Their method includes a training algorithm that utilises Kepler-K2 data to reduce false positives and true negatives. We adopt similar vetting processes used by R23 to determine a final P_{rot} measurement in the case of multiple sectors and in §4.1 we run TESSILATOR on the R23 sample and directly compare P_{rot} values. The second recent TESS code, SPINNERET (Colman et al. 2024) uses exclusively 2-minute cadence TESS data and measures P_{rot} using 2 different types of periodogram analysis and the autocorrelation method (ACF). They employ a sophisticated random forest classifier algorithm to quantify a subset of several thousand reliable periods. Similar methodologies are being considered for future TESSILATOR releases.

Since the length of a TESS sector is only ~ 27 d, and that systematic offsets are introduced when data is downlinked from the satellite, TESS struggles to measure P_{rot} for targets with $P_{\text{rot}} > 10$ d, especially for faint lightcurves. Combining data from multiple sectors is generally not possible because the instrumental response between sectors is generally non-uniform (with the exception perhaps of the TESS Continuous Viewing Zone, Hattori et al. 2022). Despite these limitations, specialised tools have been made in an attempt to improve sensitivity in the $P_{\text{rot}} \sim 10 - 15$ d range (e.g., Hedges et al. 2020; Clayton et al. 2022; Hattori et al. 2022; Holcomb et al. 2022, see Colman et al. 2024 for a detailed summary of these tools). Comparisons with targets observed in photometric missions with longer observing baselines (e.g., *Kepler*, *MEarth*, *Zwicky Transient Facility*) show P_{rot} matching rates of up to 10 per cent. We do not incorporate any of these methods in TESSILATOR, but recommend readers to try these codes for measuring longer P_{rot} with TESS data.

2.2 Why do we need TESSILATOR?

Despite the abundance of available TESS codes, TESSILATOR fills an important gap for TESS data analysis. It provides a vital resource for measuring P_{rot} values from an extremely rich, all-sky reserve of photometric data. The ease of usage, combined with the capability of analysing large catalogues of targets means TESSILATOR can provide important tests for many aspects of our understanding of stellar rotational evolution, and will contribute to tackling those major outstanding problems addressed in the first paragraph of §1. Whilst TESSILATOR can be run directly from the command line the code is entirely comprised of Python functions and all variable parameters are set as keywords that can be modified from their default values, providing users with flexibility to call individual functions into their own code. In summary, TESSILATOR has unique features compared to other available codes because of the following reasons:

- **Ease of use** – TESSILATOR can be easily installed and used directly from the command line.
- **Large target lists** – a large survey using TESSILATOR analysed > 3 million lightcurves and measured P_{rot} for ~ 1.1 million targets. The process took < 2 weeks using a moderate cluster with 208 cores (Binks et al. 2024, in preparation).
- **Treatment of contamination** – a specialised algorithm has been implemented to quantifying contaminating flux from neighbouring sources (see §3.2.1).
- **Corrections to systematics** – 2 separate routines have been developed to correct for systematic trends, if required.
- **Lightcurve vetting** – multiple functions have been created to carefully modify lightcurves and remove spurious data.
- **Periodogram analysis** – as well as performing the LSP and identifying multiple peaks as potential rotational signals, TESSILATOR also offers a specialised periodogram shuffling method to detect short periods in noisy lightcurves (see §3.4.3).
- **Outputs and products** – TESSILATOR is able to store the downloaded fits files, it provides aperture photometry, lightcurve and periodogram data, and produces informative summary plots for the analysis of each target.
- **Final period selection** – a specialised routine is offered that selects a final P_{rot} measurement in the case where a target has two or more sectors of TESS data (see §3.5.2).

3 THE TESSILATOR CODE

The TESSILATOR code, version 1.0, is available to download and the software⁵ and supporting documentation⁶ are regularly updated. We anticipate future releases that incorporate additional features, which will be largely based on feedback from users. We refer readers interested in the software architecture to the supporting documentation, which includes an application programming interface (API) with detailed descriptions for each function.

To guide the reader through the processing steps in this section, we present examples from the set 6551 TESSILATOR lightcurves for 1560 targets selected for TESS lightcurve analysis in R23. The details of the R23 sample are described in §4.1. In this section, we describe each step carried out by TESSILATOR, from quantifying contamination, performing aperture photometry, normalising, cleaning and detrending lightcurves, removing systematic flux, applying the LSP, returning quality and reliability parameters, and calculating a final P_{rot} . In each step, we outline the methods, considerations and underlying assumptions. A flow-chart outlining each step carried out in the TESSILATOR code is presented in Figure 1.

3.1 Target input and data retrieval

3.1.1 Target input

The first task is to provide TESSILATOR with input, and (if needed) perform a cross-match with the Gaia DR3 main source catalogue (Gaia Collaboration et al. 2023, which is required for assessing the background contamination, see §3.2.1). If only a single target is required, this may be passed as a command-line argument as either a resolvable target identifier or as a pair of sky coordinates. TESSILATOR can read file input in three different modes: (a) target identifiers; (b) sky coordinates; or (c) a list containing basic Gaia data.

⁴ <https://www.tessextractor.app/>

⁵ <https://github.com/alexibinks/tessilator>

⁶ <https://tessilator.readthedocs.io/en/latest/>

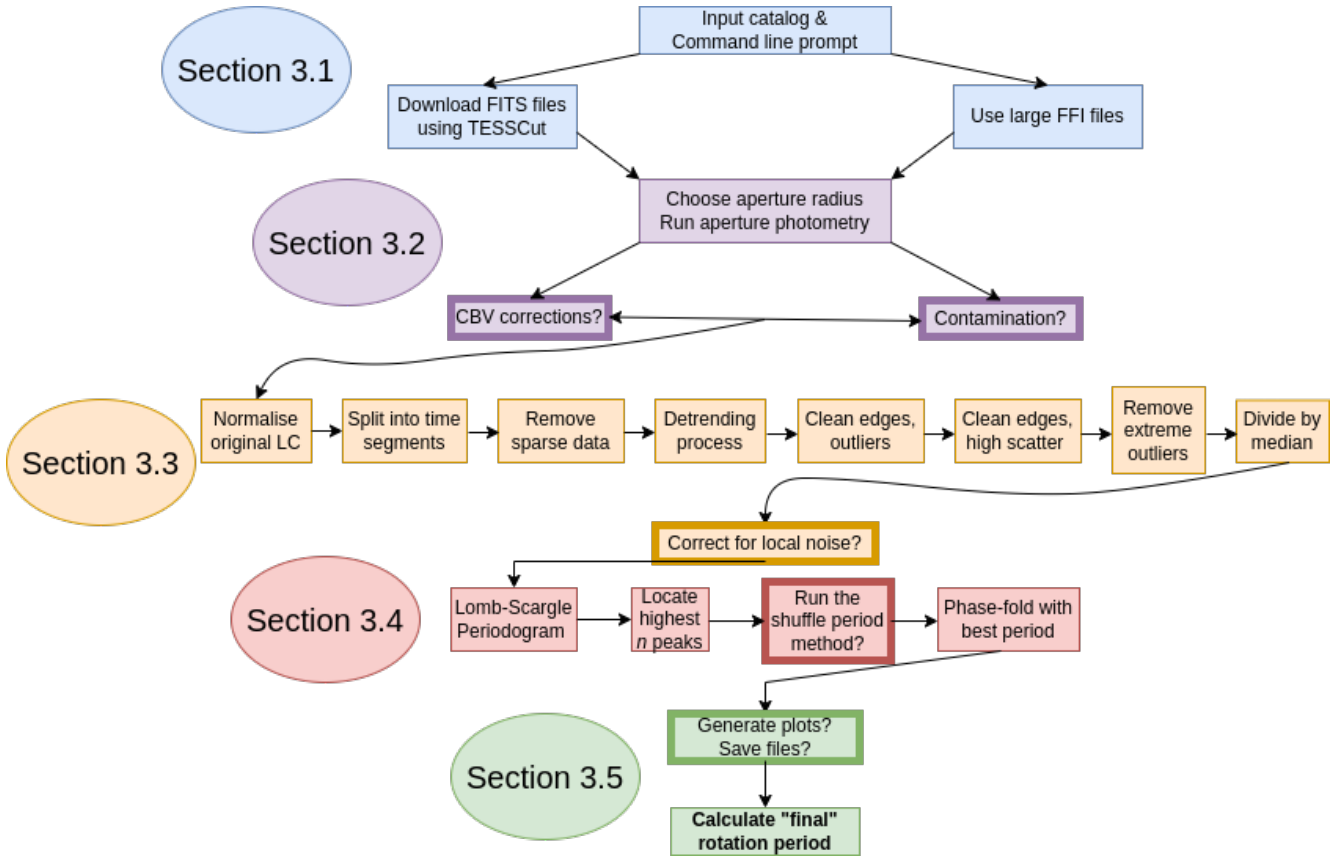


Figure 1. A flowchart depicting the procedures performed by TESSILATOR. The colours are used to group small procedures into higher-level, general steps in the code, as follows: blue=target input and data retrieval (§3.1); purple=aperture photometry (§3.2); orange=lightcurve analysis (§3.3); pink= P_{rot} calculation (§3.4) and green=“final” P_{rot} for a given target (§3.5). Inputs with bold outlines are optional steps.

3.1.2 Data retrieval

The code extracts TESS full-frame images (calibrated, FFIC) in two separate modes: either by downloading small regions of data surrounding each target of interest by using the TESSCUT software (Brasseur et al. 2019, herein, the cutout method), or by using the entire set of FFIC images for a given Sector/Camera/CCD (SCC) configuration⁷ and locating positions of target stars on these images using the TESS_STARS2PX.PY module from Burke et al. (2020, herein, the sector method). If the cutout method is chosen, the user can decide whether to collect data for all available sectors, a specified list of sectors, or simply just one sector, and also has an option to cap the number of sectors for download (this is useful when there are many TESS sectors for a given target or group of targets).

The observing cadence for the FFICs was shortened from ~30 min between sectors 1-27 (cycles 1 & 2, the primary mission), to 10 min between sectors 28-55 (cycles 3 & 4, the first extended mission) and to 200 s from sectors 56 onwards (cycles 5+, the second extended mission). For the sectors with 30 min cadence, each TESSCUT image, centered on a 21x21 pixel tile requires ~9 MB of disk space (the file size is inversely proportional with cadence), whereas the sector method for a given SCC requires ~36 GB of disk space. Therefore for surveys with ≥ 4000 targets in a given SCC, the sector method is better in terms of memory storage. However, even for projects

with slightly fewer targets one may still want to consider the sector method because of the time expense of downloading many individual sources.

Ultimately, the preferred choice of data extraction depends on the task in hand, but as a general guide, smaller or larger surveys are better suited to the cutout or sector method, respectively. The reader should note that a full sector of FFICs requires 16 times more disk space than a single SCC, because there are 4 cameras and 4 CCDs per sector. Once data has been downloaded and ingested by TESSILATOR, the subsequent processes are identical for each of these two modes.

3.2 Aperture photometry

Since the aim of TESSILATOR is primarily to analyse lightcurves for (faint) stars, we treat targets as point sources and use circular aperture photometry to calculate instrumental TESS T -band fluxes for all individual frames. Depending on the choice of FFIC data extraction, these could be from the image stack produced by TESSCUT or a list of time-ordered images from a full SCC set. We tested and confirmed that both methods would produce identical lightcurves.

Using a 21×21 pixel region with the aperture centered on the pixel closest to the given sky-position, an annulus region with inner and outer radii of 6 and 8 pixels (respectively) is used to calculate the median background flux per pixel. The chosen annuli values ensure the background contains minimal flux contribution from the source, whilst the annulus area is large enough that any bright background sources would not affect the median count.

⁷ Available for download at https://archive.stsci.edu/tess/bulk_downloads/bulk_downloads_ffic-tp-lc-dv.html

There are two options for selecting the aperture radius (r_{ap}). To calculate the amount of flux incident within the aperture, we measure the fractional area of each pixel included in the aperture, and take this fraction of the flux from each contributing pixel. The first option is to use a fixed value, which is set as default to 1.0 pixel. This, incidentally, is close to the theoretical optimum for flux extraction in the sky-limited domain (Naylor 1998). The second option uses a simple algorithm we developed called “calc_rad”, which selects r_{ap} by assessing whether the immediate neighbouring pixels (i.e., the 1-pixel border surrounding a square) contribute significant flux compared to the central pixel. This is often the case for bright stars, where $r_{\text{ap}} = 1$ would not capture enough of the source flux, and can lead to erroneous lightcurve production (see, e.g., Figure 2).

Here we describe in basic terms how “calc_rad” calculates r_{ap} . The flux values are initially background subtracted and a variable called r is set equal to 1 (representing the start of the procedure). If k_{r+1} , the ratio of the median value of the 8 neighbouring pixels and the central pixel is greater than some specified value, k_{lim} (the default value is 0.1), r increases by 1, and the flux values of the next set of 16 surrounding pixels are compared with the central pixel, and so on, until $k_{r+1} < k_{\text{lim}}$. The final value for r_{ap} is calculated by linearly interpolating between k_r and k_{r+1} , using the r and $r + 1$ values either side of the pass/fail boundary and finding the value for r where $k_r = k_{\text{lim}}$. If, after 3 iterations, the $k_r > k_{\text{lim}}$ condition is still satisfied, or if k_r increases at any point, then we suspect there might be contribution from a bright neighbouring source and we reset the final r_{ap} to 1 pixel. This algorithm is repeated for every image in the stacked data frame. Altering r_{ap} between frames would cause discontinuities in the lightcurve, therefore the median aperture radius is chosen as the final r_{ap} to be used in each image frame.

Once r_{ap} has been evaluated, aperture photometry is performed using methods from the PHOTUTILS Python package (Bradley et al. 2022). The background flux per pixel is multiplied by the aperture area to calculate the total background flux in the aperture, and T magnitudes are calculated using a zero-point of 20.44 ± 0.05 mag (Vanderspek et al. 2018). Only images with data quality flags (fits header: “DQUALITY”) set to zero are retained in the analysis. Once aperture photometry has been performed for all images, the results are stored to a table ready for further vetting. It is important to point out that when using the sector version of TESSILATOR, aperture photometry can be simultaneously performed at multiple positions on the FFICs, which significantly expedites the image processing.

3.2.1 Background contamination

Due to the large size of TESS pixels (the pixel length corresponds to an angular extent of 21”), contamination from neighbouring sources can be an important factor that reduces the signal to noise for a target source and/or can result in a false P_{rot} measurement for a target, where the true source of the P_{rot} is from a neighbouring contaminant.

To quantify the flux contribution from neighbouring sources that passes through r_{ap} (defined in §3.2), TESSILATOR performs an SQL search of the Gaia DR3 catalogue to find neighbouring sources within a given pixel distance of the target. Since the passbands and response functions for TESS T (Ricker et al. 2015) and Gaia DR3 G_{RP} (Riello et al. 2021) photometry are very similar (600 – 1000 nm), and given that the practical faint limit for measuring TESS lightcurves is much brighter than the faint limit of G_{RP} in Gaia DR3, we use G_{RP} fluxes to represent the source contamination.

The procedure is identical to Binks et al. (2022), who incorporate equation 3b-10 of Biser & Millman (1965) to calculate the amount of incident flux within a given aperture from a source at a given distance.

The only exception in TESSILATOR’s case is the use of a different Gaia filter (Gaia DR2 G -band fluxes are used in Binks et al. 2022). For practical purposes we set a faint limit for neighbouring sources at 3 magnitudes fainter than the target, and set a search radius of 10 pixels (as a default value). The program returns the (base-10 logarithm of the) flux ratio between the sum of the neighbouring sources and the target ($\Sigma\eta$) and also the brightest contaminant and the target (η_{max}). Examples of sources with low and high contamination are presented in Figure 3. Each contaminant is ordered in descending values of η and the first few of these are stored to a file (the default is 10).

An optional procedure is offered that assesses whether any of these stored contaminants might be the source of the measured P_{rot} and/or if the target P_{rot} might be deemed unreliable. Lightcurve processing and periodogram analyses are performed for each contaminant, using the exact same steps (§3.3 and §3.4) as those made for the target. Each contaminant is assigned a “false flag” and a “reliability flag”. A false flag value of 1 (or 0) is assigned if the absolute difference between the contaminant and target P_{rot} is less (more) than the quadrature sum of the P_{rot} uncertainties. The reliability flag depends on the pixel distance (d_{pix}) between the contaminant and target. If $d_{\text{pix}} < 1$, the contaminant is considered unresolved, so if the contaminant flux is greater (less) than the target flux, we deem this as unreliable (reliable) and assign a value of 1 (0). In the case where $d_{\text{pix}} > 1$, if the amplitude of the phase-folded lightcurve of the contaminant is greater (less) than half that of the original target lightcurve, we assign a value of 1 (0). If an error occurs during these tests, or if there are no contaminants, or if this option is ignored, then both flags return a value of 2, 3 or 4, respectively. These flags can be particularly useful if the target is in a crowded field or if the P_{rot} reliability is particularly important. However, the additional computation time needed scales with the number of contaminants to be assessed, and the processing of many targets in this way can become cumbersome.

3.2.2 Correcting for systematics: Cotrending Basis Vectors

During image exposures, TESS CCDs are sensitive to radiation from sources other than the targeted sky region. These contribute to a systematic flux component. Some of this systematic flux comprises of scattered diurnal and lunar light, the former of which can impart small 1-day aliasing in the lightcurves, whereas the latter contributes an additional noise term. The other systematic effect comes from the instrument response, which causes non-uniform flux sensitivity across the CCD chip. This is often due to temperature gradients across the light collecting area, especially at times just before or after data transfer when the detectors are switched off and back on. In addition, the CCD chips suffer degradation over time. Systematic flux is likely to be more problematic for targets with low signal-to-noise ratio or for targets with very low amplitudes of variability.

The TESS science team have provided tools to help reduce the systematic flux imprint. By measuring the lightcurves for many stars across each SCC, common features in the lightcurves are detected using principal component analysis. These are provided as fits tables each containing 8 co-trending basis vectors (CBVs) sampled at shorter cadences than the FFI image⁸. By applying linear fits between the CBVs and the lightcurve, the systematic flux can be removed. The CBV corrections are particularly suited to bright stars and targets whose point spread function is non-circular, and often represent an important stage in producing cleaned lightcurves for transiting

⁸ https://archive.stsci.edu/tess/bulk_downloads/bulk_downloads_cbv.html

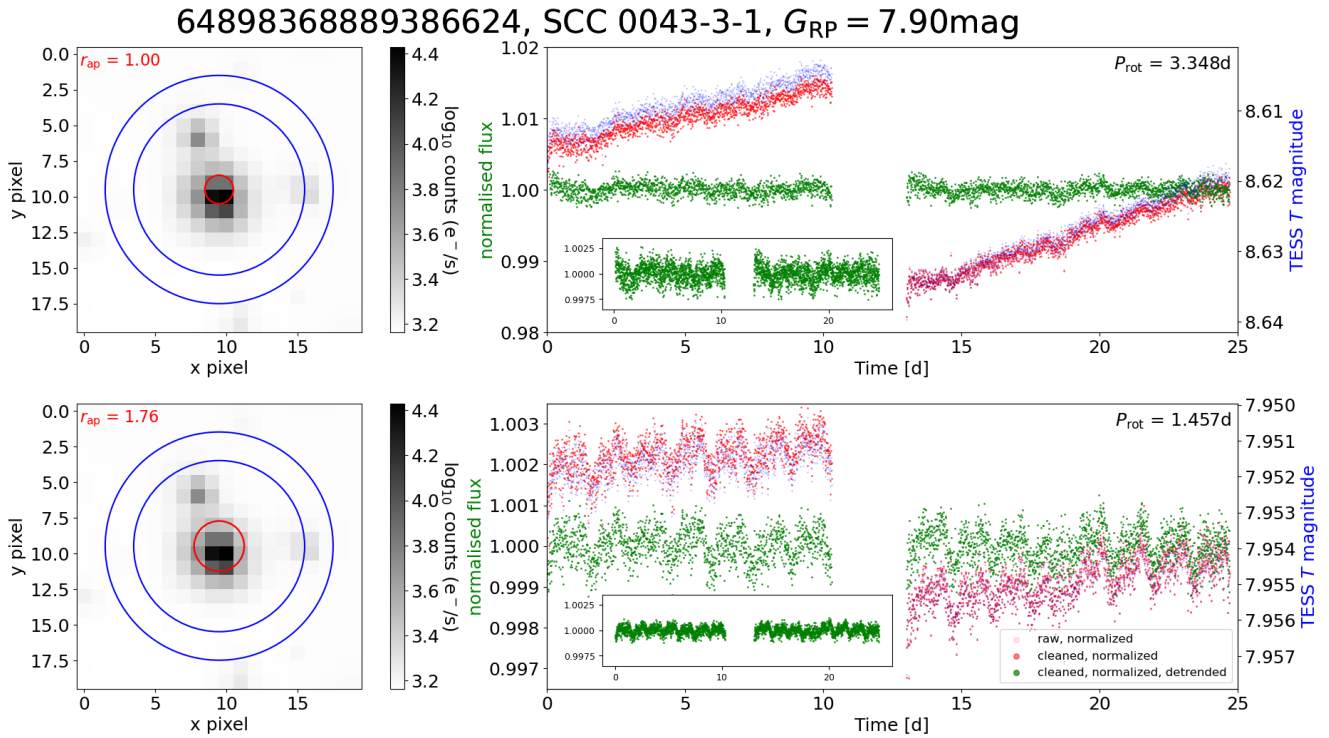


Figure 2. An example depicting how the choice of aperture radius can affect the (normalised, detrended and cleaned – green data points, see §3.3) lightcurve and P_{rot} calculation for Gaia DR3 64898368889386624 (Sector 43, Camera 3, CCD 1), a bright target with $G = 8.124\text{mag}$. The left panels show the 20x20 pixel cut-out image centered on the target, with the aperture and annuli used to evaluate the source and background flux are shown as one red and two blue circles, respectively. The right panels represent the TESS magnitude, normalised flux, and the subsequent detrended flux (see §3.3) as blue, red and green points, where the insets are both zoomed-in regions using the same range of y-values to indicate the amplitude of variability for the detrended flux. The results for a (fixed) aperture radius of 1.0 pixel, and that of a 1.76 pixel extraction (based on the algorithm described in §3.2) are displayed in the top and bottom panels, respectively. The larger aperture radius is clearly preferential, not only because the measured TESS T magnitude is better matched to the Gaia DR3 G_{RP} magnitude ($= 7.90\text{mag}$, the TESS magnitude filters are closely matched with Gaia DR3 G_{RP} , see §3.2.1), but the measured P_{rot} ($= 1.457\text{d}$) is in good agreement with the R23 value ($= 1.462\text{d}$), whereas the top panel fails to provide a match to either of these parameters.

planets (Guerrero et al. 2021) and short-term variable targets including Type Ia supernovae (Fausnaugh et al. 2021) and blazars (Poore et al. 2024). In practice, however, this technique is highly prone to overfitting, and the net effect of CBV fitting can be unwanted noise injection, or the inclusion of lightcurve features that were not initially present.

Therefore, we offer CBV fitting as an option in TESSILATOR, but advise that the user only employs CBV corrections if they are confident that the effects will improve lightcurve quality. To make the CBV corrections to the lightcurve we apply the method used by Aigrain et al. (2017), which uses a variational Bayes method to optimize the number of CBVs used in the linear fitting procedure. This maximum-likelihood method, designed for Kepler data but applicable to TESS lightcurves, is designed to be robust to overfitting and artificial noise injection.

If a user selects the CBV-correction procedure, the CBV-corrected lightcurve must pass two separate tests for it to be selected as the data to be used to calculate P_{rot} , otherwise the original lightcurve is used and this CBV-corrected lightcurve is rejected (although the CBV-corrected lightcurve can be saved to file). The first test (CBV test 1) involves comparing different features of each lightcurve before they have been passed to any of the processing steps described in §3.3, and the second test (CBV test 2) uses features from the LSP analysis, where the inputted lightcurves have been fully processed (described in §3.4). Both tests use a point scoring system based on several criteria. The CBV-corrected lightcurve must score higher than the

original lightcurve in CBV test 1 for it to qualify for CBV test 2. The two tests are described in more detail in Appendix A, since the reader will need to read sections §3.3 and §3.4 to understand the specific details of each test.

The CBV-corrected lightcurves therefore fall into three categories, which are labelled and stored as a “CBV_choice” flag. These are: CBV_choice=0 (rejected in CBV test 1); CBV_choice=1 (fails CBV test 2); or CBV_choice=2 (passes both tests). If the CBV-correction option is not selected, then CBV_choice=3. Examples of comparisons between the original and CBV-corrected lightcurves are provided in Figure 4. It is clear there are cases where the CBV-corrections serve only to inject noise and create more systematic offsets into the lightcurve (e.g., top panel), cases where the CBV-corrections improve the shape of the lightcurve, but the injection of noise causes the original lightcurve to perform better in the periodogram test (middle panel), and finally cases where the CBV-corrections provide better results (bottom panel).

To examine the typical outcome of these CBV tests, we use the Pleiades targets from R23 (sectors 42–44). Figure 5 indicates that, from a possible 2203 lightcurves, only 10 per cent (220) pass both CBV tests. Brighter targets (i.e., those with $G < 9$) are labelled “CBV pass” slightly more frequently than fainter ones (~ 23 versus ~ 9 per cent, respectively), suggesting that the typical net effect of CBV corrections for fainter sources is to inject additional noise. Therefore, we reiterate that CBV corrections should only be applied

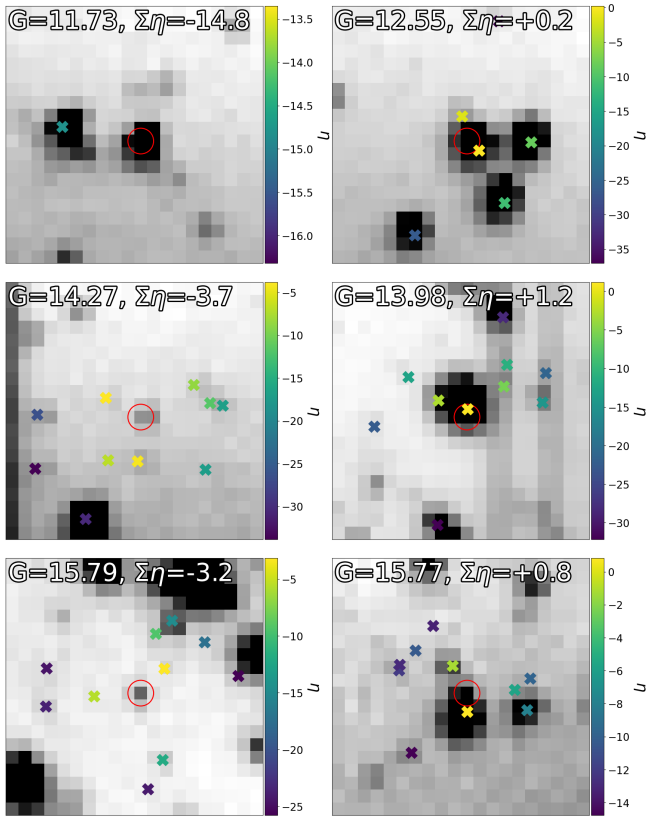


Figure 3. FFIC images for 6 targets, indicating contamination from neighbouring sources. The top, middle and lower panels represent bright ($11 < G < 13$), medium ($13 < G < 15$) and faint ($G > 15$) targets, and the left and right panels show examples of low ($\Sigma\eta < 0$) and high contamination ($\Sigma\eta > 0$), respectively. The coloured crosses on each image represent the X/Y pixel positions of the top 10 contributing contaminants, in terms of η (see §3.2.1).

if the user is confident that they result in a significant improvement to the lightcurve.

3.3 Lightcurve analysis

After performing aperture photometry and generating an initial lightcurve for a target (and applying the CBV-correction if required), TESSILATOR performs several normalisation, detrending and cleaning procedures to prepare the target for periodogram analyses. In the following sub-sections, we use examples of lightcurves in Figure 6 as a visual aid to describe the processing steps, which will follow the flowchart presented in Figure 1.

3.3.1 Normalising the original lightcurve

The lightcurves are initially normalised, by dividing all (background-subtracted) flux values by the median flux in each lightcurve. The median was selected to ensure robustness to outliers, whilst ensuring the lightcurve amplitudes are not flattened in the normalisation process. Normalised flux error bars are calculated simply by dividing flux uncertainties by their flux values.

3.3.2 Splitting data into time segments

Whilst the total time baseline per sector for a TESS sector is approximately 27 days, data acquisition for targets observed takes place across 2 parts, both equalling the length of a 13.7 day orbit. Throughout the primary mission and first extended mission (TESS cycles 1-4), data was downlinked from the satellite, typically in $\sim 1 - 2$ days, whilst close to perigee. Since the second extended mission began (TESS cycles 5+) the data acquisition strategy changed slightly, such that data is downlinked every ~ 7 days, causing 3 gaps, but each with substantially shorter downtime.

During the downlink, the satellite must also perform additional maintenance and engineering tasks such as momentum dumps to ensure the orbit remains stabilised. Therefore the data gap duration changes from sector to sector. We refer to each group of data observed between these gaps as “segments”. As the CCDs switch observing modes, electronic signals cause temperature variations across the detectors, and this instrumental response frequently leads to discontinuities at the end points of each segment. In addition, across each observing segment, gradual flux gradients are often seen. Figure 6 highlights an example of the features described in the former and the latter, in the second panel of the $9 < G < 12$ group and the top panel of the $12 < G < 15$ group, respectively.

In order to vet the lightcurves, and remove systematic trends, we must first group the data by their segments. These are defined as sets of contiguous data points whose neighbouring data points are separated in time by no more than 10 times the median time difference. Using this method almost always returns 2 or 4 segments (depending on the TESS mission when the observations were taken), however there are also cases where additional time gaps exist due to excluding poor quality data in the aperture photometry, or simply gaps due to the satellite failing to record photometry, both of which can result in a different number of segments.

3.3.3 Removing sparse data

Any segments from lightcurves comprising of 2 or more segments that have very few data points (N_{seg}) should be removed, as these are typically very scattered and only contribute noise to the lightcurve. We developed a method to remove the sparse data. Firstly, we require a segment to contain at least a minimum number of data points, N_{thr} , which is selected as the maximum value between 5 per cent of the total number of data points in the lightcurve and 50 (both of which are default values in the code). For lightcurves with > 2 segments, we calculate the standard deviation of N_{seg} values, and if this is larger than N_{thr} , we retain only the segments where $N_{\text{seg}} > N_{\text{thr}}$.

This method ensures we remove very sparse data, whilst retaining > 90 per cent of the data. In Figure 6, the first target in the $9 < G < 12$ group has 3 segments of data, where the middle segment contains relatively very few data points. We found that the gap between the first and second segment does not represent the downlink, but actually a time period where several data anomaly flags were returned.

3.3.4 The detrending process

As mentioned in §3.3.2, the (flux-normalised) TESS lightcurves often exhibit flux gradients across each segment (due to the instrument response), and clear discontinuities at the start/end points between neighbouring segments. If the lightcurves are left like this, there is a strong risk that an LSP analysis (or any other P_{rot} measuring method) could calculate an incorrect, usually much longer P_{rot} value, because

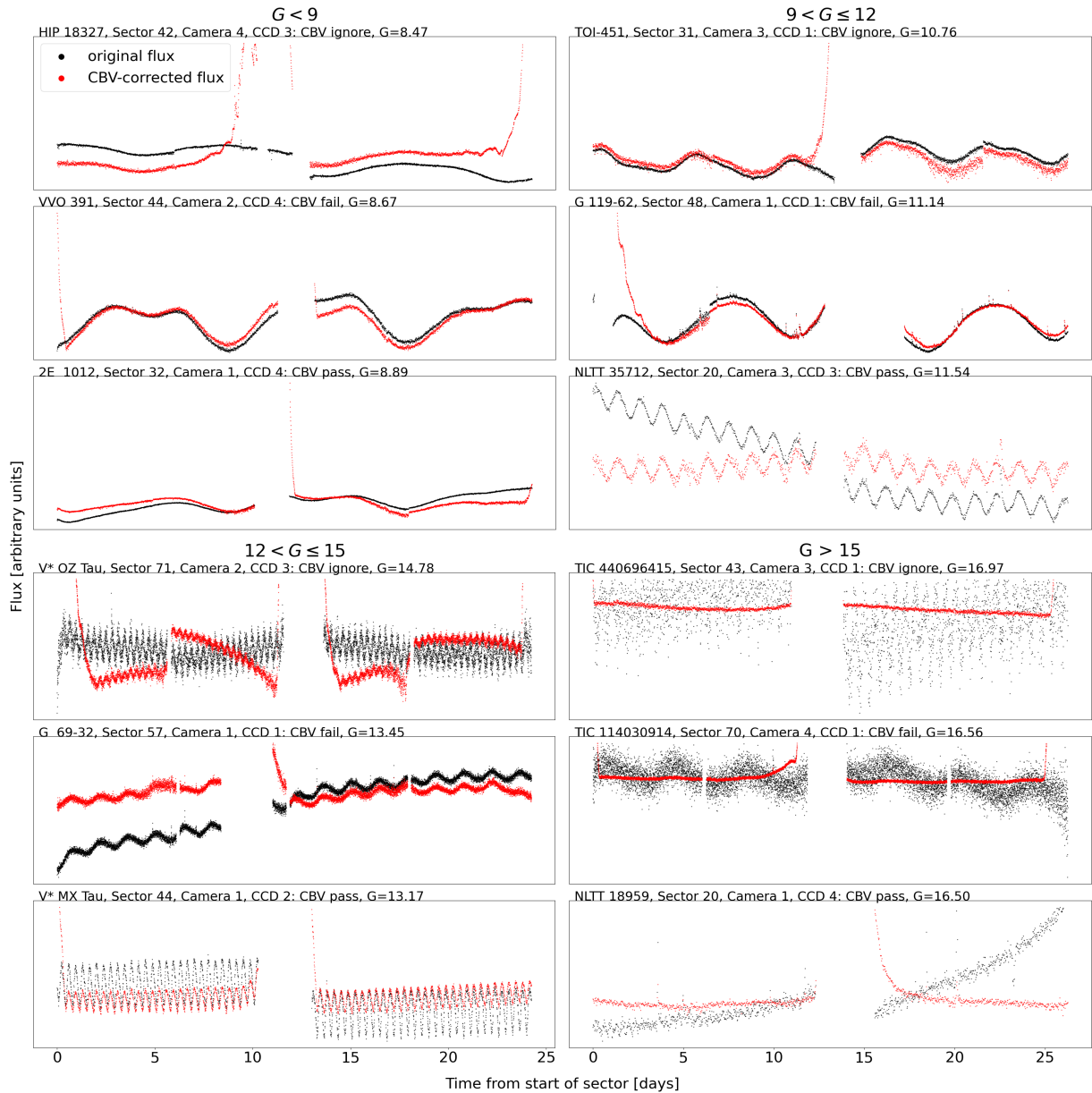


Figure 4. Examples of lightcurve of targets selected from R23, in the cases where the CBV-corrected lightcurve: fails CBV test 1 (“CBV ignore”, first and fourth row), passes CBV test 1, but fails CBV test 2 (“CBV fail”, second and fifth row); or passes both tests (“CBV pass”, third and sixth row). The data from the original fluxes and the CBV-corrected fluxes are highlighted in black and red, respectively. The “CBV ignore” example in the $G < 9$ set typifies an example of severe over-fitting, where clearly the CBV-corrections result in worse lightcurves. The third and sixth row show that even when both tests pass, the CBV corrected lightcurves sometimes have unphysical spikes near the edges that are not present in the original lightcurves.

the jump in flux from one segment to the next may result in significant power output at lower frequencies during the Fourier transform. For these lightcurves, detrending is a crucial step.

A clear example of when detrending is necessary is presented in the top panels of Figure 7 for TIC 302923006 (Gaia DR3 662003860752394880, see Figure 6, $G > 15$ group, second panel). From visual inspection of the lightcurve, this target clearly has a P_{rot} value around ~ 1.1 d, however, without the detrending step, the LSP analysis returns a much longer P_{rot} value (~ 14.8 d).

However, detrending does not always lead to improved lightcurves. In some (rare) cases, for targets with longer P_{rot} (e.g., > 10 d), the lightcurves may have sufficiently small systematic offsets during data gaps and the lightcurve is better without any detrending. An example

of this is shown in the lower panels of Figure 7 for HD 251108, which displays a clear $P_{\text{rot}} \sim 20$ d (this target has $P_{\text{rot}} = 21.18$ d in the AAVSO International Variable Star Index VSX catalog, [Watson et al. 2006](#)). Because of the different ways that a lightcurve might be manifested, TESSILATOR runs several routines to determine if a lightcurve should be detrended.

For our detrending function, we make a polynomial fit of the form $f_{\text{fit}} = \sum_0^N p_n t^n$, for $N = 0$ and $N = 1$. The value of N is chosen using the Aikake Information Criterion (AIC) by comparing the sum of least squares for both fits. If the AIC value for $N = 0$ is smaller, then this polynomial is used for detrending, otherwise the polynomial fit for $N = 1$ is used. The reason for rejecting any higher order polynomials is because they would flatten the signal in

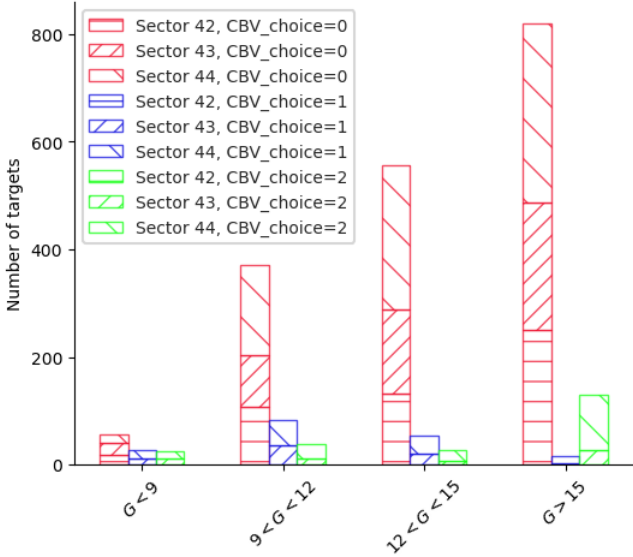


Figure 5. A bar chart representing the proportion of Pleiades targets from R23 that have CBV_choice labels of either 0 (fail CBV test 1), 1 (fail CBV test 2) or 2 (passes both tests). These results are separated into 4 Gaia DR3 G magnitudes ranges and 3 TESS sectors (42, 43 and 44). The brightest sample ($G < 9$) contains the largest fraction of lightcurves labelled as “CBV pass” (~ 23 per cent), whereas all other samples have much lower fractions (all $\lesssim 10$ per cent). These numbers are fairly constant in each sector, suggesting that the CBV tests do not depend on the sector.

lightcurves if the fit traced the shape the lightcurve, and also because they risk injecting periodicity in flat lightcurves (e.g., those that do not exhibit any periodic signal in the first place).

Step 1 – smoothing

The first part of the detrending process is to decide how to detrend the lightcurve (if at all), which begins with determining if the lightcurve has properties like HD 251108 (meaning no detrending should be performed at all). The idea is to make a sinusoidal fit to the data, and measure how good the fit is. The 5 steps for this process use parameters that have been selected through a trial and error process to maximise true positives and false negatives. They are:

- (1) Detrend the whole lightcurve using a linear fit, and calculate the normal-scaled median absolute deviation (herein, simply referred to as “MAD”) of the detrended flux values (f_{MAD}).
- (2) Fit a sinusoidal function to the detrended lightcurve of the form $f_{\text{norm}} = f_0 + A \sin\left(\frac{2\pi}{P_{\text{rot}}}t + \phi\right)$, where the parameters to be fit are f_0 (a constant), A (the amplitude), P_{rot} (the rotation period) and ϕ (the phase) and t represents the time coordinate.
- (3) Smooth the time and flux arrays using a boxcar of 10 data points (this is to remove short timescale irregular features such as flares).
- (4) Subtract the smoothed lightcurve by the sine fit and calculate the MAD (d_{MAD}).
- (5) Calculate the relative root mean squared error (RRMSE) between the detrended flux and the sine fit (f_{RRMSE}).

If the period from the sine fit is > 15 d, $f_{\text{RRMSE}} < 0.01$ and $d_{\text{MAD}}/f_{\text{MAD}} < 0.25$, then the lightcurve is considered to be like HD 251108 and no detrending is made to the lightcurve. The output from this step is a boolean flag called “smooth_flag”.

Step 2 – normalisation choice If “smooth_flag” is False, then neighbouring segments of the lightcurve are assessed to determine if they are significantly offset, or if they would suitably connect. Another boolean flag called “norm_flag” is initially set to False. Treating two consecutive segments A and B , we provide a least-squares linear fit to both (S_A and S_B), and calculate the predicted (extrapolated) flux value from S_A at the first data point of B (B_0), and compare this with the predicted value from S_B . We then detrend A and B (using S_A and S_B) and calculate the MAD flux for each. If the absolute difference between S_A and S_B at B_0 ($|\Delta AB|$) is greater than twice the mean MAD value (m), then “norm_flag” is set to True, and all segments of the lightcurve are detrended individually and the routine is stopped. Otherwise if there are > 2 segments, the process is repeated for pairs B and C , and so on. The lightcurve is detrended as a whole only if all pairs satisfy the condition that $|\Delta AB| < m$.

3.3.5 Cleaning the segment edges: outliers

There are sometimes cases at the start and end parts of each segment where the flux values increase or decrease by an amount much larger than the typical scatter in the rest of the lightcurve. This is likely due to temperature changes in the detectors when they are switched off/on during data downlink. These often contribute a significant amount of noise, and removing these data points should lead to a cleaner lightcurve.

Therefore TESSILATOR uses a basic algorithm to remove the flux “tails”. After the detrending processes are complete, the flux values for each segment are passed to the segment edge cleaning routine, and the median and MAD flux is calculated. Then from either edge of the segment (moving forwards and backwards in time from the start and end points, respectively), we check if the absolute difference in flux between the data point and the median is less than twice the MAD value. If not, the data point is rejected, and the test continues until a data point satisfies the condition. A clear example of this algorithm working in practice can be seen in the third panel of the $12 < G < 15$ group in Figure 6, where several data points at the end of each segment are removed (displayed as grey data points) because they have a sharp rise in flux.

3.3.6 Cleaning the segment edges: scattered data

As well as the flux tails described in §3.3.5, the scatter amongst local flux values in regions close to the segment edges are sometimes significantly more scattered in relation to the rest of the segment. This may be a result of the detectors stabilising as the observations begin and/or end. Scattered data at the edges of segments can potentially contribute another noise term to the lightcurve, and removing them should lead to a cleaner lightcurve.

TESSILATOR provides a method to remove the scattered data by comparing the localised scatter with the rest of the segment. The method was developed with the intention to remove extreme data points, without removing potentially useful data. The idea is to select N data points and calculate a running mean of the MAD values across the segment, where the value for N is chosen as the lower value of either 0.01 times the number of data points in the segment or 11. If N is even, we add one to it, so we can pad both edges of the running mean array with $(N - 1)/2$ data points (the padded values are twice the MAD flux for the whole segment). We will denote this array as f_{mean} .

The median absolute difference in flux between 2 neighbouring data points across the whole segment is calculated, which we denote

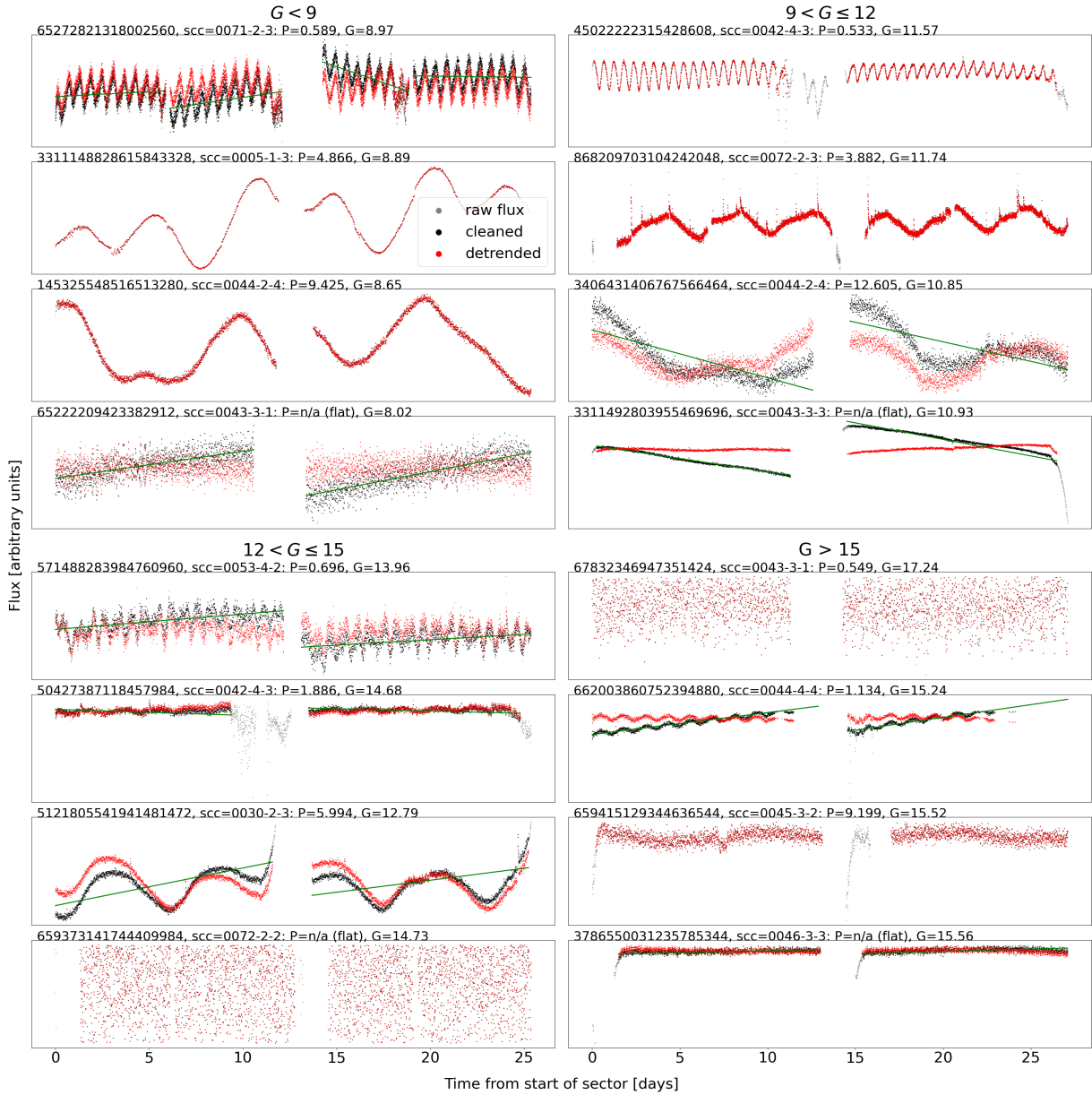


Figure 6. A gallery of TESSILATOR lightcurves for 16 targets, selected to provide visual aids to help explain the processes described for the lightcurve analysis in §3.3. The top-left, top-right, bottom-left and bottom right quadrants of the gallery represent 4 brightness regimes (in terms of Gaia DR3 G mag). For each brightness quadrant, in the first, second and third panels we show a fast, medium and slow rotator (where P_{rot} is < 1 d, between $1 - 5$ d and > 5 d, respectively), and the bottom panel represents a lightcurve with an indeterminate P_{rot} . Grey and black dots indicate the normalised flux before any processing (raw flux) and after the cleaning steps. Green lines indicate any detrending functions (if used), and the red symbols represent the data that constitutes the final lightcurve.

as f_{diff} . Then, from either edge of the segment (moving forwards and backwards in time from the start and end points, respectively) we test the condition $f_{\text{mean}} < 2f_{\text{diff}}$. If the condition is not satisfied, we repeat for the next value of f_{mean} in the array until we have a match, which marks where we set the start and end points of the segment. If the condition is immediately satisfied, we assume the segment edges have no significant extra scatter and no cleaning is performed. The same target used to demonstrate the edge outlier cleaning method (§3.3.5) can also be used to show the edge scatter cleaning method. At the end of the first segment it is clear that additional data points are removed because of large localised scatter. An example of the removal of highly scattered data at the edges of lightcurve segments can be seen in the second panel of the $12 < G < 15$ group in Figure 6.

3.3.7 Removing extreme outliers

At this stage in the lightcurve analysis, the data has been normalised, segmented, detrended and cleaned. We then remove any remaining data points with flux values that can be considered as extreme outliers. To do so, we measure the median and MAD flux, and remove data points with flux values that are > 5 MAD from the median flux. We note that the datapoints classed here as extreme outliers may be astrophysical in nature, for example optical flares (Günther et al. 2020) and/or accretion-driven bursts in young T-Tauri systems (Lin et al. 2023). In future TESSILATOR releases we plan to incorporate lightcurve smoothing functions, from which the residuals could be used to identify flares and classify flare properties.

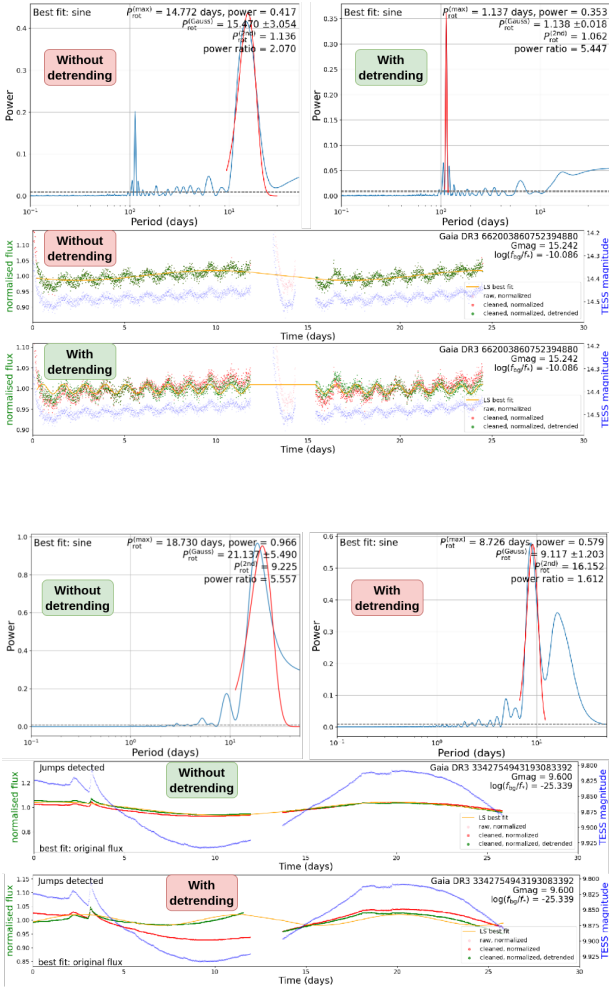


Figure 7. The effects of the detrending process on the LSP for two different lightcurves. The lightcurve in the top panel (TIC 302923006, Figure 6, $G > 15$ sample, second panel) shows a $P_{\text{rot}} = 1.1$ d is easy to confirm by visual inspection. However, because of the flux discontinuities between sectors, without any detrending, the LSP analysis predicts a longer P_{rot} (~ 15 d, left panel). When the detrending process is included, the expected P_{rot} value is recovered (right panel). The bottom panel represents a lightcurve for a target (HD 251108) where detrending would lead to an incorrect P_{rot} . Note that this target has been previously measured with $P_{\text{rot}} = 21.18$ d (Watson et al. 2006).

3.3.8 Final normalisation step

The final step is to divide the detrended flux in each segment by the median detrended flux for all data points in the segment that pass the cleaning steps in §3.3.3, §3.3.5, §3.3.6 and §3.3.7. This concludes the processing steps for the lightcurve.

3.3.9 Returning the processed lightcurve

The lightcurve processing method generates two products: a table of lightcurve data to be passed to further steps such as the LSP analysis (see §3.4) and a dictionary of parameters calculated in the detrending process (§3.3.4). Both these products can be saved to file.

If the CBV-correction method is selected (see §3.2.2) then the two products are made for both the original and the CBV-corrected fluxes. The lightcurve table retains information for all data points, regardless of whether or not they pass the 4 cleaning steps in the

lightcurve analysis. The first 4 columns are the time stamp, TESS T magnitude, input flux and the input flux error (directly taken from the results in §3.2). Then the subsequent columns are the normalised flux and error (from §3.3.1), an index number used to group the segments (§3.3.2), a qualification flag for sparse data (§3.3.3), the detrended flux (§3.3.4), and qualification flags from cleaning the segment edges from outliers (§3.3.5) and scatter (§3.3.6) and the extreme outlier removal (§3.3.7), and the median-divided final flux to be used for LSP analysis (§3.3.8).

3.3.10 Additional lightcurve quality flags

Once the lightcurve has passed through the processing steps, 2 optional procedures are offered, both of which return a boolean flag that classify some additional lightcurves feature. The first tests if there appear to be significant discontinuities amongst neighbouring data points in a lightcurve segment. This might be a result of the instrumental response at the ends of each segment, but could also indicate a flare event or some other activity-related phenomenon. Therefore, we provide a “jump_flag” for each lightcurve, which may prove useful for users depending on their reasons for using TESSILATOR. Our flagging algorithm simply constructs an array of the running average of 10 consecutive flux values, which we label “ A_{run} ”, and another array containing the absolute difference in neighbouring A_{run} values, which we label “ A_{diff} ”. A “jumpy” lightcurve is one in which the ratio of the maximum and median values in A_{diff} becomes greater than 10 at any point across the segments.

The second procedure assesses whether the lightcurve is best matched to a sinusoidal or a linear fit. If the former is found, then the rotational signal likely strong enough to be detected, whereas the latter case suggests that the lightcurve is flat or noisy. Since there are 3 fixed parameters in the sinusoidal fit compared to 2 in the linear fit, the Aikaake Information Criterion is used to decide which of the least-squares fit is the most appropriate.

3.3.11 Noise corrections using real data

We provide an alternative method for correcting instrumental systematics, by using the neighbouring targets identified as potential contaminants in §3.2.1. For the method to run, the contamination calculation must be performed and there needs to be at least one contaminant identified in the image area. Each potential contaminant is passed through the same procedures as the target, and for each time stamp, a median-flux value is calculated from all contaminants that satisfy all qualification criteria in §3.3. The corrected target flux is calculated by dividing the final flux by the median contaminant flux at each time stamp.

This process is most effective when there are lots of nearby potential contaminants that have flat lightcurves, and in practice it is up to the user to decide if and when to apply this correction.

3.4 Periodogram Analysis

Whilst there are many methods to measure P_{rot} from photometric data, such as the autocorrelation method (ACF), wavelet transformations and Gaussian processes (to name just a few, see §1), TESSILATOR only uses the Lomb-Scargle periodogram (LSP) method⁹. The basic procedure for the LSP is to find a best least-squares sinusoidal

⁹ We have experimented with using ACF, and we are considering providing ACF and/or other methods as an option in a future version of the software.

fit to a lightcurve, using a grid of frequencies. Since LSP uses a simple linear regression to fit sinusoids, the computation time can be relatively fast, especially when Fast Fourier Transform algorithms are applied and an informed choice of frequency grid spacing and sampling factors is chosen. It is capable of measuring P_{rot} with unevenly sampled data (unlike ACF methods), and the periodogram output (a normalised power spectrum as a function of P_{rot}) encodes important information across a wide range of input P_{rot} values, allowing us to investigate not just the P_{rot} , but other sources of variability (e.g., accretion, magnetic activity, spot modulation).

The P_{rot} value corresponding to the maximum power is not necessarily the true P_{rot} , for (at least) 2 reasons. The first involves the details of spot modulation. The angular resolution of TESS is far too large to resolve any surface features from a target. Therefore the cause of the flux variations is unknown, but generally assumed to be the migration of spots across the stellar disk. Although we assume a constant rotational speed for the spots, the monitoring of Sunspots (e.g. Carrington 1863), and spots on Solar-like stars (e.g. Brun & Browning 2017) show a clear latitude dependency, with the fastest and slowest spots found at the equator and poles, respectively. This means the measured P_{rot} may be erroneous, or even meaningless, if a star has significant differential rotation. If the migration of spots from the Northern and Southern hemispheres are coherently out of phase as they move across the disk, the measured P_{rot} can be mistaken as half the true P_{rot} , i.e., the spots are double-counted.

The second reason comes from the way the LSP deals with noisy and/or flat lightcurves. For these lightcurves the LSP may falsely yield a large power output at long P_{rot} (typically > 10 d). This is mainly because small, gradual variations in flux across long timescales (e.g., across the entire sector) will have a higher sensitivity in the LSP, especially if there is no/little variability in the lightcurve on short timescales. In many of these cases, we can use some of the lightcurve properties and results from the LSP to reject them as poor data or at least flag them as spurious results. These “quality indicators” are described in §3.5.

3.4.1 Implementing the Lomb-Scargle Periodogram calculation

We use the `LOMBSCARGLE` python module (Astropy Collaboration et al. 2022) with the auto-power method selected as an optimal compromise between accuracy and computational speed. An important step is to sample a frequency (or P_{rot}) grid that is relevant for TESS lightcurves. With this in mind we select boundaries that correspond to $P_{\text{rot}} = 0.05$ d and 100 d, respectively. The rationale for the lower limit is that the TESS/FFIC observing cadence is $\sim 0.007 - 0.021$ d ($\sim 10 - 30$ min, depending on the TESS mission mode during data acquisition). This ensures our frequency sampling rate is well below the Nyquist limit. In addition, low-mass stars are very rarely observed with $P_{\text{rot}} < 0.2$ d (McQuillan et al. 2013; Ramsay et al. 2020), therefore this lower limit ensures we can detect ultra-fast rotators. The upper limit was chosen because the duration of a TESS sector is ~ 27 d, therefore reliable P_{rot} measurements are typically limited to $< 10 - 12$ d. However, we set our upper limit at $P_{\text{rot}} = 100$ d because we need to fit error bars for lightcurves with longer P_{rot} . Setting a sampling rate of 10 points for each frequency node results in a grid of ~ 6000 points. The typical spacing in P_{rot}/d is $\sim 0.003, 0.1$ and 0.4 at P_{rot}/d values of 1, 5 and 10, respectively.

The data selected for the LSP are described in §3.3.9, with the time, flux and flux error provided as input, which will herein be denoted simply as t , f and σ_f , respectively. After running the LSP, the P_{rot} and normalised power output (herein simply “power”) are recorded, and saved to file if necessary. Using the value of the maximum power

output, False Alarm Probability (FAP) powers are then calculated assuming a null hypothesis of non-varying data with Gaussian noise at the 0.1, 1.0 and 5.0 per cent level, based on the method described by Baluev (2008).

3.4.2 Fitting Gaussian profiles to the highest n peaks

In §3.4 we explained why the highest power output of the LSP may not represent the true P_{rot} . Therefore we designed a method to return P_{rot} values from the highest n power outputs from distinct peaks in the LSP, where we set $n = 4$.

The method works by identifying the array index corresponding to the maximum power output, and counting all neighbouring preceding and subsequent indices with power values that decrease monotonically until there is an inflection and the power value increases. The LSP power spectra for lightcurves that are noisy or possessing multiple components can sometimes have peaks that are asymmetric, and the top of these peaks can be double-humped. Therefore we make an exceptional rule that if a data point has a power value > 85 per cent of the maximum power, we allow the program to continue running even if the new power value represents an increase.

The P_{rot} and power values between the start and the end index from this method are used to make a Gaussian fit. The centroid and full-width half maximum are used to provide a Gaussian P_{rot} and uncertainty. This information is saved, and these parts of the LSP are removed. The process is then repeated n times for the desired number of LSP peaks.

3.4.3 The shuffled period method

The general LSP method, as described in §3.4.1, uses lightcurve data measured over a full TESS sector. As we have discussed, a reliable P_{rot} measurement necessitates a lightcurve in which the stellar rotation provides the dominant signal. Despite considerable normalisation, detrending and cleaning steps (see §3.3), signals from the systematics, sky background and non-periodic surface features may dominate those from the underlying rotation, especially for faint sources with low signal to noise.

A visual inspection of some TESSILATOR-produced lightcurves for faint sources with short P_{rot} (≤ 3 d, as measured by Kepler-K2, Howell et al. 2014) show that the rotational signal is undulating and apparent. However the LSP for these targets often return relatively little power at the correct P_{rot} , because other components – usually with much lower frequency – dominate the signal.

We have developed a specialised LSP method, specifically designed to measure P_{rot} in cases where the amplitude of the rotational signal is too small to be detected when the full sector of lightcurve data is used. The general idea is to randomly sample many lightcurve subsets across the sector and measure their P_{rot} . If the distribution of P_{rot} values from these randomly sampled subsets has a small-enough variance, then its mean value, which we denote as P_{shuff} , replaces the P_{rot} corresponding to the LSP peak power output across the full sector. Specifically, there are 5 steps to the method:

(1) Measuring P_{rot} for many subsets of the lightcurve.

We select 5000 randomised subsets of lightcurve data from the whole sector. The data for each subset is chosen by: (a) randomly selecting a lightcurve segment (see §3.3.2); (b) extracting a random fraction, f , of the chosen segment, between 0.1 and 1; and (c) selecting the starting point of the subset as a random fraction between 0 and $1 - f$ of the segment. Each subset is linearly de-trended, and the LSP is performed as described in §3.4.1, but with a maximum P_{rot} set to

4 times the duration of the subset. This yields 5000 sampled P_{rot} measurements (herein P_S).

(2) **Constructing a histogram of P_S .**

The first histogram (H_1) represents a broad fit of all P_S values, which is used to find the P_{rot} bounds of the distribution surrounding the most populated bin. The P_S are placed onto a base-10 logarithmic scale, and split into 50 equal-spaced bins.

(3) **Identifying the P_{rot} range surrounding the peak of H_1 .**

Using the algorithm described in the second paragraph of §3.4.2 (here we replace the power output with the number occupancy in each bin and we set the “exception rule” as 5 times the median number occupancy), we measure P_{S_L} and P_{S_U} , which are the P_S lower and upper values that represent the bounds of the region surrounding the maximum occupancy value. The fraction of the total P_S that lie within P_{S_L} and P_{S_U} (which we label f_1) is calculated, and a second, refined histogram (H_2) is produced, this time using 10 times the number of bins that (at least partially) lie within P_{S_L} and P_{S_U} , normalised such that they summate to 1.

(4) **Applying the first set of criteria.**

The criteria that must be matched for P_{shuff} to remain in consideration are: (a) the number of H_2 bins that lie entirely within P_{S_L} and P_{S_U} must be > 3 ; (b) $f_1 > 0.5$; and (c) the H_2 peak must not be in a bin that overlaps with P_{S_L} and P_{S_U} . The process only continues if these conditions pass, otherwise the P_{shuff} is rejected.

(5) **Applying the second set of criteria.**

We make a Gaussian fit to the binned data in H_2 , and measure the relative root mean square error (RRMSE). At this stage we calculate the value of P_{shuff} and uncertainty from the Gaussian fit parameters. The second set of criteria that must be matched in order to replace P_{rot} with P_{shuff} are: (a) $\text{RRMSE} < 0.5$; (b) the full-width half maximum of the Gaussian fit < 0.05 ; and (c) $|1 - (P_{\text{shuff}}/P_{\text{rot}})| > 0.1$.

Figure 8 provides an example of when P_{shuff} is, and is not adopted. Generally, if there is a clear, rapidly rotating P_{shuff} , then the scatter in P_S is very small, meaning the number of false positives is very low. We note that this method is particularly effective at detecting P_{rot} in lightcurves with low-amplitude for rapid rotators, or at least P_{rot} shorter than the duration of a typical segment. However, the shuffle method is not capable of finding longer P_{rot} , given that the P_{shuff} values are never longer than the time duration of a segment.

3.4.4 Phase-folded lightcurves

A phase-folded lightcurve (PFL) is formed by simply dividing the time coordinates by the selected P_{rot} . Displaying the lightcurve in this format allows one to visualise repeating patterns in a P_{rot} cycle such as rotational modulation, transits, eclipses or accretion events, which may be less easy to identify in the full lightcurve. Each time coordinate is zero-shifted (such that the first datapoint is equal to zero), and then divided by P_{rot} . The whole part and decimal part of these transformed values represent the number of cycles and the phase, respectively.

We measure four quantities from the PFL, which are used to help assess the reliability of the P_{rot} measurement. The first two of these are a measure of the amplitude (A) and scatter (s) of a sinusoidal fit to the PFL, of the form $f_{\text{fit}} = A \sin(2\pi t + \phi) + f_0$, where ϕ and f_0 represent the phase and a constant, respectively. To measure s , we calculate a value $\rho = f/f_{\text{fit}}$, then split the PFL into ten equal phase sections and calculate the mean ($\bar{\rho}$) and standard deviation (σ_ρ) for each section. Finally, s is given as the median σ_ρ over the ten sections. The third quantity is a reduced χ^2 score for the sinusoidal fit, and

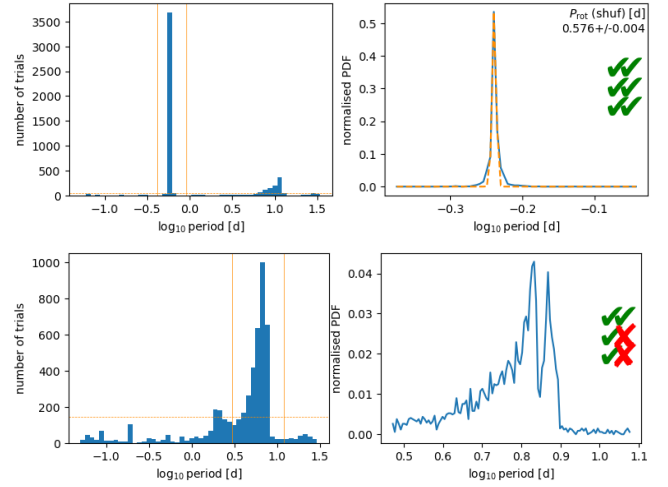


Figure 8. An example of the results of the P_{rot} histograms for a case where the shuffled P_{rot} is selected (top panel) and another where some criteria fail, and therefore P_{shuff} is not used (see §3.4.3 for details). The left panels show the initial P_S distribution, where the orange horizontal line indicates $5\times$ the median bin occupancy, and the orange vertical lines show the resulting P_{S_L} and P_{S_U} bounds (see step 3 in the routine) that are used to construct the refined P_{shuff} histogram, shown on the right. The target in the upper panel satisfies all 6 criteria and the target in the lower panel fails 2 criteria (b and c in step 5).

the fourth is the fraction of data points with $|f - f_{\text{fit}}| > 3 \times f_{\text{MAD}}$, which we deem as extreme outliers.

3.5 Outputs, quality indicators and calculating a final P_{rot}

Once TESSILATOR has completed the procedures in §3.1, §3.2, §3.3 and §3.4 (see Figure 1), a results table for all measured parameters of a given lightcurve is returned, which may be saved to file. Table 1 provides details for each of the columns of this results file, which consist of general Gaia and TESS demographic information, details on the background contamination, boolean flags from the lightcurve vetting, and outputs from the periodogram analysis and phase-folding. If required, a plot summarising the main results is provided. An example of a TESSILATOR summary plot is shown in Figure 9.

3.5.1 Quality indicators

The quality and reliability of a TESS lightcurve depends on many factors. These are typically based on: the flux ratio between the target and surrounding background and/or neighbouring contaminants; the instrumental response in a given SCC; and the physical parameters and surface features of the target. For these reasons, TESSILATOR measures several quantities that can be used to assess the quality and reliability of the lightcurve, as described in Table 1. Here we mostly focus on the criteria used in §4.1 to vet the 6551 lightcurves used for the comparison with R23.

For the background contamination, we suggest flagging lightcurves with “log_tot_bg_star” > 0 as potentially unreliable. This is because the background contaminants would represent at least half of the flux in the aperture, making it difficult to determine the source of any rotational modulation. Of course, it is possible to further study

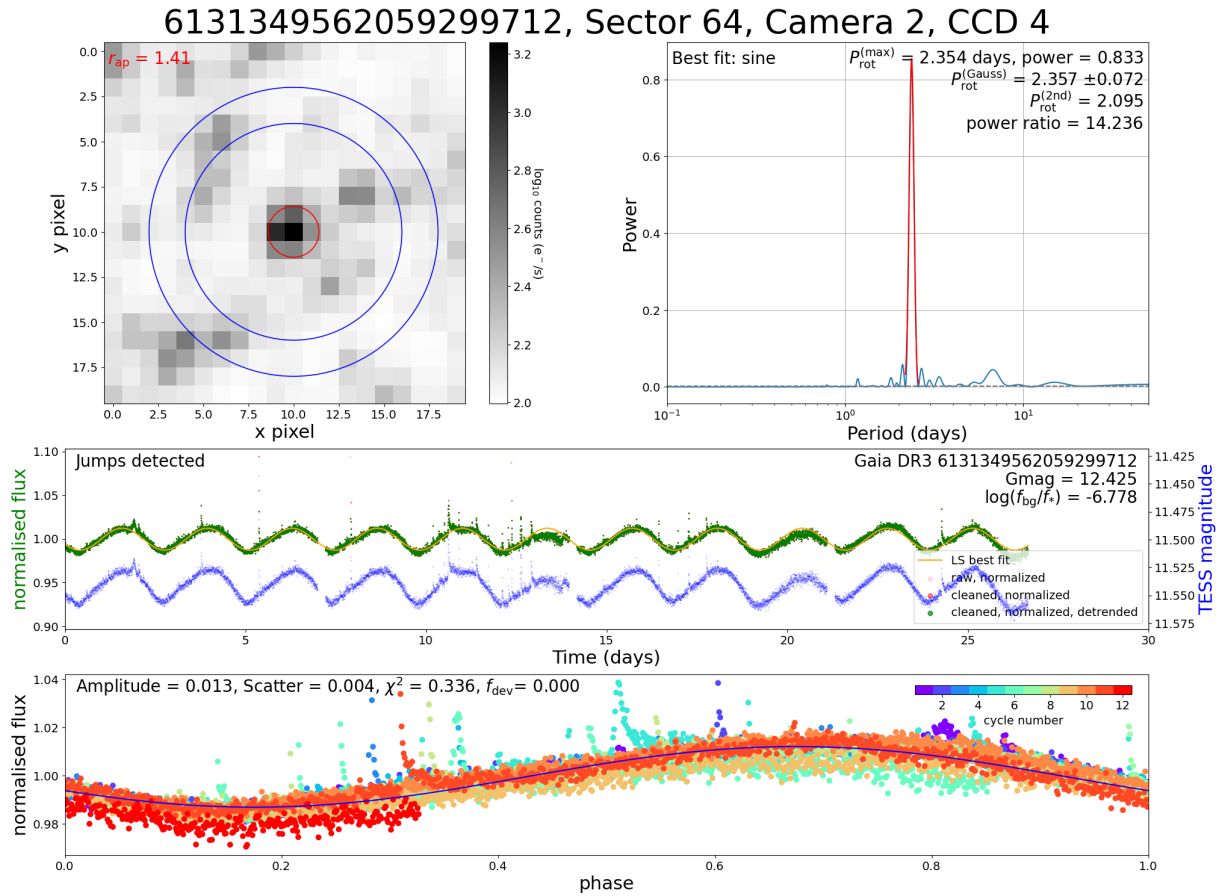


Figure 9. A plot generated with TESSILATOR, which displays the main results of the processing steps described in §3. The title gives the original_id and SCC. Top-left: a 20×20 pixel cutout from the middle slice of the TESS image stack, with the greyscale representing the range of base-10 logarithmic counts. The red inner circle represents the aperture radius (the value is given in the top left) and the blue circles are the annuli used to calculate the background. Middle: the lightcurve created by TESSILATOR, where blue points represent the TESS magnitudes calculated during aperture photometry and pink, red and green points represent the normalised fluxes in: their original form; after detrending; and those that pass the cleaning processes. The orange line represents a best-fit sinusoid, calculated during the LSP analysis. Top-right: Results from the LSP analysis, where the red section indicates the region around the selected P_{rot} . The dashed horizontal line near Power=0.0 represents the power output of the FAP at 1 per cent. Bottom: the green lightcurve from the middle panel phase-folded using the selected P_{rot} . A rainbow colormap indicates the cycle of each phase throughout the sector, and the blue curve represents the best-fit sine function to the phase-folded lightcurve.

the effects of each contaminant source if required, using the “false” and “reliable” flags.

Although the lightcurve analysis provides quality criteria on whether the lightcurve contains jumps (“jump_flag”) and the flatness (“AIC_line” and “AIC_sine”), we do not consider these as strong quality criteria. This is particularly important for the latter criteria, since it removes many faint targets with low SNR.

The outputs from the LSP provide several important quality indicators. The ratio between the power of the LSP peak and the power corresponding to the FAP at 1 per cent should be sufficiently large, the P_{rot} uncertainty should be relatively small, and long P_{rot} values should be treated with caution.

The details from the phase-folded lightcurve provide important criteria. The ratio of the amplitude and scatter can be set to a minimum threshold to avoid noisy, flat lightcurves. Additionally, if the amplitude or the scatter is very large, this may be indicative of a poor lightcurve. Finally, the “chisq_phase” and “fdev” values can be set, such that they should not exceed maximum values.

The choice of quality criteria are largely subjective and depend on the requirements of the user. For example, if faint targets are

being analysed, then the amplitude is likely to be low (so a criteria based on amplitude should be relaxed), or if a target is in a crowded field, one may wish to relax the criteria for contamination. In future work we plan to experiment further with these quality criteria using machine learning tools such as random forest classifiers to determine the relative importance of these features.

3.5.2 Calculating a final P_{rot}

The task of calculating a final P_{rot} (herein, P_{fin}) for a target when there are lightcurves from 2 or more sectors is not trivial. Before we describe our method, we note that TESSILATOR does not measure differential rotation (nor indicate them). For small datasets we recommend that users visually inspect lightcurves and apply intuition to ensure reliable P_{fin} values. However, for large target samples, or even when there are many sectors of data for just one target, an automated method for measuring P_{fin} is preferable.

Our method is largely adopted from sections 3.1 and 3.2 in R23, which consists of two steps: determining the P_{rot} value to be selected

Column name	Description
General properties	
original_id	Target identifier (§3.1.1)
source_id	Gaia DR3 source identifier
ra	Right ascension (epoch J2000)
dec	Declination (epoch J2000)
parallax	Gaia DR3 parallax
Gmag	Gaia DR3 G -band magnitude
BPmag	Gaia DR3 G_{BP} -band magnitude
RPmag	Gaia DR3 G_{RP} -band magnitude
Tmag_MED	Median TESS T -band magnitude (§3.2)
Tmag_MAD	MAD TESS T -band magnitude (§3.2)
Sector	TESS sector number
Camera	TESS camera number
CCD	TESS CCD number
Background contamination	
log_tot_bg	$\Sigma\eta$ (§3.2.1)
log_max_bg	η_{\max} (§3.2.1)
num_tot_bg	Number of contaminating sources
false_flag	Test if a contaminant is the P_{rot} source (§3.2.1)
reliable_flag	Test if the P_{rot} source is reliable (§3.2.1)
Lightcurve properties	
CBV_flag	The CBV-correction category (§3.2.2)
smooth_flag	Flag for detrending step 1 (§3.3.4)
norm_flag	Flag for detrending step 2 (§3.3.4)
jump_flag	Test for jumps in the lightcurve (§3.3.10)
AIC_line	AIC score: linear fit to the lightcurve (§3.3.10)
AIC_sine	AIC score: sine fit to the lightcurve (§3.3.10)
Periodogram analysis	
Ndata	Number of datapoints in the periodogram analysis
FAP_001	1% False Alarm Probability power (§3.4)
period_1	Primary P_{rot} (peak)
period_1_fit	Primary P_{rot} (Gaussian fit centroid)
period_1_err	Primary P_{rot} uncertainty
power_1	Power output of the primary P_{rot}
period_2	Secondary P_{rot} (peak)
period_2_fit	Secondary P_{rot} (Gaussian fit centroid)
period_2_err	Secondary P_{rot} uncertainty
power_2	Power output of the secondary P_{rot}
period_3	Tertiary P_{rot} (peak)
period_3_fit	Tertiary P_{rot} (Gaussian fit centroid)
period_3_err	Tertiary P_{rot} uncertainty
power_3	Power output of the tertiary P_{rot}
period_4	Quaternary P_{rot} (peak)
period_4_fit	Quaternary P_{rot} (Gaussian fit centroid)
period_4_err	Quaternary P_{rot} uncertainty
power_4	Power output of the quaternary P_{rot}
period_shuffle	P_{shuff} (§3.4.3)
period_shuffle_err	Uncertainty in P_{shuff} (§3.4.3)
shuffle_flag	Indicates if P_{shuff} was adopted (§3.4.3)
Phase-folded lightcurve details	
amp	Amplitude of the PFL (§3.4.4)
scatter	Scatter of the PFL (§3.4.4)
chisq_phase	χ^2 value of the sinusoidal fit to the PFL (§3.4.4)
fdev	Number of extreme outliers in the PFL (§3.4.4)

Table 1. The names and description of each column in the results table. When necessary, we refer the reader to the appropriate section in this manuscript for more details.

from each individual lightcurve (P_{sec}) and calculating P_{fin} using all the P_{sec} values.

Step 1 – Determining P_{rot} for a single lightcurve (P_{sec})

For lightcurves with clear, unambiguous rotational modulation, the selected P_{sec} is usually the P_{rot} value corresponding to the highest peak of the LSP (herein $P_{\text{rot},1}$). However, this is not always the case. There two cases where an alternative P_{rot} may be selected for P_{sec} . As described in §3.4.2, TESSILATOR provides P_{rot} for the highest n peaks from the LSP, where the default is $n = 4$.

The first case relates to slow rotators. For the purpose of our automated P_{sec} measurement, we remove any P_{rot} values > 20 d. Whilst this means our pipeline is unable to identify targets with $P_{\text{sec}} > 20$ d, we find that TESS, with sectors only lasting ~ 27 d, is usually incapable of measuring rotation slower than this. We find it more favourable in general to eliminate false positives in this way. In almost all cases, the TESS lightcurves for targets whose P_{rot} values are *known* to be > 20 d (from surveys with longer observing baselines) appear very flat, and therefore are eliminated due to some quality criteria failure (see §3.5.1).

The second case accounts for potential double-counting of spots, which can lead to estimates of P_{rot} that are half the true value (Basri & Nguyen 2018). As in R23, we select an alternative P_{rot} from the $n \geq 2$ set if this matches twice the $P_{\text{rot},1}$ value (within one error bar of the alternative P_{rot}) and the power corresponding to this peak is > 0.6 that of $P_{\text{rot},1}$.

Step 2 – Determining the final P_{rot} value (P_{fin})

The P_{sec} values, errors and corresponding power output values, selected in step 1, are used to calculate P_{fin} . How P_{fin} is calculated depends on whether the number of P_{sec} values (N_{sec}), is 1, 2, or > 2 .

For $N_{\text{sec}} = 1$, P_{fin} is obviously equal to P_{sec} and no further analysis is needed. For $N_{\text{sec}} = 2$, we first check if one P_{sec} is approximately double that of the other. If the difference between the longest P_{sec} and twice the shortest P_{sec} is less than either the mean of both error bars or 10 per cent of the shortest P_{rot} , then P_{fin} is selected as the longest P_{sec} . Otherwise, P_{fin} is the power-weighted mean of both measurements.

Determining P_{fin} for $N_{\text{sec}} > 2$ is slightly more complex. Like in the $N_{\text{sec}} = 2$ case, we need to check if any of the P_{sec} measurements in the set are double values. The first step is to measure the median P_{sec} (P_{med}) and the corresponding error bar ($\sigma_{P_{\text{med}}}$). Then we determine which lightcurves have either a half or full P_{sec} within one $\sigma_{P_{\text{med}}}$ value of P_{med} . The final chosen P_{fin} depends on whether more than two-thirds of these match this criterion.

- If $\geq 2/3$ satisfy the criterion, only use sectors that represent matches. If there are no “half” matches in this set, then P_{fin} is the power-weighted mean. Otherwise, ensure the P_{sec} values match the double value (by doubling their P_{sec} and errors if necessary) and take P_{fin} as the median value.

- Otherwise, take P_{fin} as the power-weighted mean P_{sec} from all the individual P_{sec} values.

Selecting P_{fin} in this way allows us to utilise as much TESS data for multiple sectors, and also makes the code more likely to select the correct “double value” for P_{fin} in cases where there are measurements that are different by factors of 2. We reiterate that our goal here is to develop an automated method to calculate P_{fin} for large numbers of lightcurves. It works in most cases, but there will inevitably be some occasions where this method is not optimal. We advise the user to visually inspect lightcurves for best results.

4 COMPARISON WITH LITERATURE SAMPLES

4.1 The Rampalli et al. 2023 sample

4.1.1 Running TESSILATOR on the R23 sample

To validate our software as a tool capable of correctly measuring periods, we run TESSILATOR on the sample of 1560 stars targeted by R23. A number of these R23 targets are used as exemplars to demonstrate the TESSILATOR procedures throughout §3. The R23 target list comprises members of 5 different groups: the Pisces-Eridani kinematic stream (Pis-Eri); the Pleiades, Hyades and Praesepe open clusters; and the M-Earth sample of nearby field M-stars. The first 4 of these groups are $\sim 100 - 700$ Myr, which is an epoch where we expect the majority of stars to rotate faster than ~ 10 d (Barnes 2003; Gallet & Bouvier 2013; Angus et al. 2019) and therefore capable of having P_{rot} correctly measured with TESS data. The M-Earth sample provides a useful case study for targets that are likely to have a true $P_{\text{rot}} > 10$ d. TESS lightcurves are available for at least one target across every TESS sector (from 1-72) and most targets have multiple sectors of data. The magnitude range of the full sample is $6 < G < 18$, and the spectral-type range spans early-A to late-M.

This makes the R23 sample ideal for testing TESSILATOR’s performance across a large parameter space. All targets in the R23 sample themselves have a P_{rot} comparison with a literature source (this set we denote as “R23_lit”), which we will additionally test the TESSILATOR with. In particular, the provenance of the literature P_{rot} for the 3 open clusters is the *Kepler-K2* survey, allowing for a comparative study between different satellite photometric missions. Details of each group are summarised in table 1 of R23.

To expedite our code, we ran TESSILATOR as a parallel-processing task, using the “bwForCluster BinAC” facility at the Baden-Württemberg Center for High Performance Computing¹⁰. We set a limit of no more than 10 sectors of data per target and decided not to apply any CBV corrections. The run split the target list of 1560 equally among 90 cores, each of which was allocated 1Gb of RAM. The job completed in approximately 5 hours. The run produced output for 6551 lightcurves for 1543 targets (for 17 targets there are no lightcurves because TESSILATOR ran into either an SQL server issue, or the lightcurve analysis failed to run).

4.1.2 Fixed TESSILATOR criteria for R23

Our first test is to determine if we should apply a set of fixed quality criteria to vet the lightcurves (see Table 1 for a description of the parameters). If P_{shuff} is used (i.e., “shuffle_flag”=1), then no additional criteria are applied (except $P_{\text{shuff}} > 0.1$), otherwise we set the following criteria:

- $\log_{\text{tot_bg}} < 0$
- $\text{period_1_err}/\text{period_1} < 0.25$
- $0.1 < \text{period_1} < 20.0$
- $\text{chisq_phase} < 0.4$
- $\text{scatter} < 0.1$
- $\text{amp} < 0.2$
- $\text{fdev} < 0.01$

With these criteria applied, we lose about 30 per cent of the lightcurves (1967 in total) and 116 targets, leaving us with 4557 lightcurves (687 with shuffle_flag=1) and 1429 targets.

¹⁰ <https://uni-tuebingen.de/en/einrichtungen/zentrum-fuer-datenverarbeitung/dienstleistungen/server/computing/resources/bwforcluster-binac/>

Our aim is to find the number of targets that have matching P_{fin} values between TESSILATOR and R23/R23_lit measurements. To do so, we measure the modulus of the difference between the period measurements, and assume that a successful match is achieved when this is less than either twice the uncertainty in P_{fin} or 0.1 d, where the latter ensures a match for very fast rotators when the P_{fin} error is very small. The total fraction of matches across all 5 groups (which we label f_{tot}), if the above criteria are, or are not implemented, is almost identical for the R23 and R23_lit samples: ~ 67 per cent (966/1429 and 1034/1543) and ~ 62 per cent (912/1436 and 949/1543), respectively. Both results suggest the effect of applying the above criteria has negligible effect whatsoever on the lightcurve quality, but it reduces the number of stars that we get P_{rot} for.

4.1.3 Variable TESSILATOR criteria for R23

In general, enforcing more restrictive criteria should result in fewer targets, but a higher fraction of matches. To test this, we employ two further criteria, but this time we make the pass threshold variable. These are the ratios of “amp” and “scatter” (herein AS), and “power_1” and “FAP_001” (PF). Table 2 represents a grid of results for various critical values of each ratio. It generally appears that a higher AS and PF value improve f_{tot} for both samples by approximately 10 per cent, however, this comes at the cost of losing almost two-thirds of the initial sample. We see that that highest values of f_{tot} are actually somewhere in the range of $2.0 < \text{AS} < 3.0$, whereas PF has an almost negligible effect on f_{tot} except at very high values (i.e., ≥ 50). A comparison of the R23 and R23_lit results indicate that when $\text{PF} < 50$, for $\text{AS} \leq 1$, $1 < \text{AS} < 3$ and $\text{AS} > 3$, the R23_lit f_{tot} are typically $\sim 0.01 - 0.04$ lower, $\sim 0.01 - 0.02$ higher, and about equal, respectively. These results suggest that AS and PF could be strongly correlated, therefore we drop PF as a criterion.

4.1.4 Results for individual groups in R23

Our next step is to see how these results look for individual groups. To do so, we apply the fixed criteria, and vary AS in the same way as we did in §4.1.3. Figure 10 shows how the fraction of matched targets (f_{grp}) and the fraction of recovered targets (f_{rec}) changes in each group as a function of AS. As expected, f_{rec} decreases monotonically with increasing AS.

In both samples, the two youngest groups, Psi-Eri (100 Myr) and Pleiades (125 Myr), have the highest f_{grp} yield for any value of AS. For Pis-Eri, $f_{\text{grp}} = 0.86 - 0.88$ at $\text{AS}=0$. This increases gradually to ~ 0.90 at $\text{AS}=4$, however, at this stage f_{rec} is only 40 per cent. Therefore, a high yield of f_{tot} and f_{rec} can be recovered at a relatively low value for AS (≤ 1.5) before f_{rec} sharply declines. Similar results are found for the Pleiades, where in both samples there is a steady increase in f_{grp} from $\sim 0.76 - 0.78$ to ~ 0.85 between $\text{AS}=0$ and $\text{AS}=4$. The decline in f_{rec} is less sharp than the Psi-Eri case, dropping to ~ 0.65 at $\text{AS}=4$.

The two intermediate-aged groups, Hyades and Praesepe (both ~ 700 Myr) have mixed results. For the Hyades, we find that f_{grp} starts at a value of ~ 0.65 and ~ 0.5 in the R23 and R23_lit sample, respectively. They both sharply rise to $f_{\text{grp}} = 0.82 - 0.84$ at $\text{AS}=2$, and remain within ~ 0.03 of this value between $\text{AS}=2$ and $\text{AS}=4$. The value of f_{rec} falls in a linear fashion down to ~ 0.45 . In the case of Praesepe, in both samples f_{grp} begins around 0.55. For the R23 sample, f_{grp} gradually increases to 0.7 at $\text{AS}=4$. For the R23_lit sample, f_{grp} increases to a maximum value of ~ 0.8 at $\text{AS}=2$. However, this is followed by a gradual decrease to ~ 0.7 at $\text{AS}=4$. We

AS	FP=0	FP=1	FP=5	FP=10	FP=50	FP=100
Comparison with R23						
0.0	966/1429=0.68	960/1419=0.68	935/1363=0.69	912/1288=0.71	763/1028=0.74	573/771=0.74
0.5	896/1267=0.71	896/1267=0.71	896/1265=0.71	891/1246=0.72	762/1028=0.74	573/771=0.74
1.0	829/1095=0.76	829/1095=0.76	829/1095=0.76	829/1094=0.76	739/971=0.76	570/768=0.76
1.5	766/990=0.77	766/990=0.77	766/990=0.77	766/990=0.77	720/923=0.78	526/679=0.77
2.0	718/887=0.81	718/887=0.81	718/887=0.81	718/887=0.81	674/840=0.80	477/603=0.79
2.5	654/797=0.82	654/797=0.82	654/797=0.82	654/797=0.82	619/761=0.81	448/566=0.79
3.0	599/732=0.82	599/732=0.82	599/732=0.82	599/732=0.82	569/701=0.81	433/545=0.81
3.5	550/674=0.82	550/674=0.82	550/674=0.82	550/674=0.82	525/648=0.81	420/530=0.79
4.0	508/628=0.81	508/628=0.81	508/628=0.81	508/628=0.81	489/608=0.80	406/514=0.79
Comparison with literature sources in R23						
0.0	912 (-0.04)	911 (-0.04)	889 (-0.03)	876 (-0.03)	756 (+0.00)	565 (-0.01)
0.5	877 (-0.02)	877 (-0.02)	877 (-0.02)	874 (-0.02)	756 (+0.00)	565 (-0.01)
1.0	821 (-0.02)	821 (-0.02)	821 (-0.02)	821 (-0.01)	740 (+0.00)	563 (-0.03)
1.5	784 (+0.02)	784 (+0.02)	784 (+0.02)	784 (+0.02)	738 (+0.02)	525 (+0.00)
2.0	732 (+0.02)	732 (+0.02)	732 (+0.02)	732 (+0.02)	692 (+0.02)	472 (-0.01)
2.5	661 (+0.01)	661 (+0.01)	661 (+0.01)	661 (+0.01)	627 (+0.01)	441 (-0.01)
3.0	602 (+0.00)	602 (+0.00)	602 (+0.00)	602 (+0.00)	573 (+0.01)	423 (-0.03)
3.5	550 (+0.00)	550 (+0.00)	550 (+0.00)	550 (+0.00)	525 (+0.00)	409 (-0.02)
4.0	505 (-0.01)	505 (-0.01)	505 (-0.01)	505 (-0.01)	486 (+0.00)	393 (-0.03)

Table 2. Results for the period matching criterion when the variable criteria “AS” and “PF” are applied for the R23 (top) and R23_lit (bottom) sample. In the top panel, the denominator is the number of targets that satisfy both the fixed criteria (see §4.1.2) and have AS and PF values above the given threshold. The numerator is the number of these targets that satisfy the period matching criterion. Since the values for the denominator are the same for the R23_lit sample we provide only the value of the numerator, and the brackets represent the fractional difference between R23 and R23_lit in a given AS/PF cell.

note that f_{rec} falls very sharply, eventually to around 0.2 (the lowest of all the groups). However, we do not think the decrease in f_{grp} is related to low-number statistics, as there are $\sim 70 - 90$ targets between $3 < \text{AS} < 4$, which is similar to the number of Hyades targets in this AS range. Rather, we identify around a dozen cases where the R23_lit P_{rot} is double the TESSILATOR P_{fin} , and 3 cases where this is > 5 times larger.

The M-Earth targets in the R23 and R23_lit samples show similar results in the way f_{grp} changes with AS, but the R23_lit are typically 0.05 – 0.15 lower. The R23 and R23_lit sample start at 0.65 and 0.5, respectively, both rising to a maximum value around AS=2, where f_{grp} is 0.77 and 0.7. These values both slightly decrease by ~ 0.03 by AS=4. The f_{rec} values gradually decrease down to ~ 0.6 and 0.55, respectively. It is possible that the R23 sample is in slightly better agreement with TESSILATOR because both use TESS data, whereas the R23_lit values use data with much longer observing baseline.

Finally, we present the P_{fin} comparisons for TESSILATOR versus R23 and TESSILATOR versus R23_lit in Figures 11 and 12, respectively. Based on the results of Figure 10, we select AP=2.0, which is typically around the maximum yield of f_{grp} for groups in each sample, and ensures the f_{rec} remains relatively large. We also find that the period matches are not correlated in any particular way with Gaia DR3 G magnitude.

The results of the period comparison are provided in Table 3. The P_{fin} column contains two sources of uncertainty: firstly, the typical measurement error from all the sectors used to construct P_{rot} , and secondly, the standard deviation in P_{sec} (after modification from accounting for half-matches). In this table we also provide a value labelled N_{half} , which provides the number of P_{sec} values that were subsequently doubled following the procedure to obtain P_{fin} (see step 2 in §3.5.2).

Interestingly, comparing TESSILATOR with the R23 and R23_lit sample, we find broadly similar f_{grp} values for Psi-Eri, Pleiades and the Hyades, but for Praesepe, f_{grp} is 0.83 in the R23_lit sample,

compared to 0.66 in R23, which are significantly different fractions at a confidence level > 99 per cent. There appear to be ~ 25 targets in the Praesepe R23 comparison that are mismatches close to either the 1:2 or 2:1 lines. It may be that we would obtain similar f_{grp} values if these were on the equivalence line, however, we also count around a dozen similar targets in the R23_lit comparison. Therefore, we suspect this discrepancy lies in the methods by which P_{fin} is calculated. Finally, for the M-Earth sample we note that f_{grp} is slightly larger in R23 than R23_lit (157/199 versus 142/199, marginally significant with a 90 per cent confidence interval). Figure 12 shows ~ 40 M-Earth targets with R23_lit P_{rot} between 10 and 150 d. Since M-Earth is a ground-based survey, as a final check, we overlay some of the 1-d alias failure models using equation 47 in VanderPlas (2018), finding very few targets that lie close to these harmonic aliases. Since the observing baseline in the M-Earth mission is several hundreds of days, we believe these to be the true period, which indicates that TESS is incapable measuring a correct P_{rot} in this range.

4.2 Large field-star P_{rot} surveys

As described in the introduction, the past few years have witnessed an exponential growth in the number of targets with P_{rot} measurements, with the vast majority coming from wide-field variability surveys that target mostly solar-type and low-mass field stars. Since the P_{rot} of a main-sequence low-mass star is usually at least 10 d (Amard et al. 2019), surveys such as *Kepler* or the Zwicky Transient Facility (ZTF), with typically year-long observing windows, are very well suited to measuring P_{rot} for these targets. On the other hand, TESS sectors span no more than 27 days and periods can only be reliably measured up to about half of a TESS sector. Whilst efforts are ongoing to “stitch” sectors (Hattori et al. 2022; Claytor et al. 2024), time-variable instrument degradation and systematic offsets has revealed this to be a highly problematic, if not impossible task.

Nevertheless, it remains a pertinent exercise to test the TESSILA-

Group	TIC	G	G_{BP}	G_{RP}	$P_{rot,lit}$	$P_{rot,R23}$	$P_{rot,fin}$	N_{half}	N_{pass}	N_{sec}
psieri	365332374	12.040	12.541	11.363	4.4	4.444	$4.428 \pm 0.262 \pm 0.038$	0	5	5
hyades	242985065	15.084	16.984	13.784	0.87	0.869	$0.864 \pm 0.010 \pm 0.006$	0	2	2
hyades	242944633	9.769	10.342	9.056	11.66	12.658	$8.817 \pm 1.424 \pm 1.887$	0	2	3
hyades	242991771	13.339	15.029	12.044	2.66	2.632	$2.664 \pm 0.099 \pm 0.008$	0	2	2
hyades	242946125	8.745	9.195	8.134	9.82	9.709	$9.793 \pm 1.434 \pm 0.142$	0	3	3
hyades	456863710	9.211	9.664	8.584	11.59	0.261	$0.521 \pm 0.002 \pm 0.001$	0	5	5
pleiades	67785558	11.569	12.079	10.886	0.5332	0.533	0.535 ± 0.003		1	1
hyades	311151814	7.706	7.999	7.246	7.47	7.692	7.567 ± 0.760		1	1
hyades	348664634	9.604	10.135	8.924	11.6	5.525	$5.653 \pm 0.465 \pm 0.158$	0	2	2
hyades	435883224	8.108	8.502	7.542	5.52	6.173	6.291 ± 0.610		1	1

Table 3. The P_{rot} measurements from our TESSILATOR analysis compared with those published in R23, for targets that satisfy the fixed and variable criteria in §4.1.2 and §4.1.3. Columns 1 and 2 provide the name of the individual group and the numeric part of the source identifier in the TESS Input Catalogue (TIC). Columns 3, 4 and 5 represent the Gaia DR3 G , G_{BP} and G_{RP} photometric magnitudes, respectively. The P_{rot} values from the literature source used as comparison in R23, and the measurements published by R23 are given in columns 6 and 7, respectively. Column 8 represents the final P_{rot} value derived by TESSILATOR, where the two uncertainty components comprise firstly of the typical measurement error from each individual sector used and secondly of the standard deviation in the P_{rot} values. Finally columns 9, 10 and 11 are the number of lightcurves that appear to have half-values of P_{rot} , the number of sectors used to construct $P_{rot,fin}$ and the number of sectors with P_{rot} measurements prior to selecting P_{fin} , respectively. Only the first 10 entries are given here, whereby the full sample of 887 targets is made available in electronic format.

Survey	Instrument	P_{rot}	G
McQuillan et al. 2013, M13	Kepler	0.3-50	9.5-16.2
Newton et al. 2016, N16	MEarth	0.1-100+	7.2-16.9
Angus et al. 2018, A18	Kepler	1-80	8.1-19.3
Oelkers et al. 2018, O18	TESS	0.5-50	4.8-12.9
Reinhold & Hekker 2020, R20	TESS	1.2-30	11.2-17.3
Santos et al. 2019, S19	Kepler	0.4-100+	9.7-17.7
Santos et al. 2021, S21	Kepler	0.4-100+	9.7-17.7
Holcomb et al. 2022, H22	TESS	0.3-20	5.3-16.2
Lu et al. 2022, L22	ZTF	1-100+	13.2-17.9
Colman et al. 2024, C24	TESS	0.5-10	5.2-16.1

Table 4. Basic properties of the 10 field-star surveys selected for analysis with TESSILATOR. Columns 3 and 4 denote the approximate literature P_{rot} and G -band magnitude range from the 1000 randomly selected targets in each survey.

TOR using several of the recently published field-star P_{rot} surveys. This can help inform us about the results one could expect when TESSILATOR fails because either a target has a P_{rot} too long to be detected by TESS, or the sensitivity-limits and/or contamination makes a TESS analysis unfeasible. We have randomly selected 1000 stars each from 10 catalogues, which represent a mixture of observing facilities and stellar properties (spectral-type, brightness, variability). A brief summary of these surveys is presented in Table 4. For simplification, we refer to each survey using the shortened form, provided in column 1.

We run the TESSILATOR using the target identifiers given in the literature source. This is to avoid any ambiguity in coordinate matches, and ensures we measure P_{rot} for the correct target. The TESSILATOR is run using all the default parameters (without considerations for CBV corrections). The same selection criteria used to obtain final P_{rot} values from TESSILATOR in §4.1 are used, as are the conditions to satisfy a matching P_{rot} with the literature value.

The results of the P_{rot} comparison are presented in Figure 13. There are some visually apparent features in the plot that merit comment. Firstly, it is clear that the fraction of matching P_{rot} values decreases with longer P_{rot} , and because of the limit imposed in our initial selection criteria to measure a P_{rot} for each TESS sector, there are no matches when the literature P_{rot} is longer than 20 d. Although

TESSILATOR analyses 1000 targets in each survey, there are usually far fewer that end up having a TESSILATOR P_{rot} measurement (even before applying criteria), because there are many noisy, flat lightcurves where TESSILATOR predicts a long, but unreliable P_{rot} . In general, the percentage of matches (f_{match}) significantly improves when the criteria are applied, however, with the exception of C24, this comes at the expense of losing more than 3 quarters of the initial matches.

The panels with the highest f_{match} (with criteria applied) tend to be those where the literature source also uses TESS data (e.g., $f_{match} > 0.5$ in R20, H22 and C24). The notable exception is O18, where f_{match} is only 38 per cent. We note that many of these targets seem to fall close to the 1-day alias failure modes (VanderPlas 2018), and suggest that, because scattered diurnal light is more of an issue in the first few TESS sectors (Vanderspek et al. 2018), this may go some way to resolving the discrepancy seen here, where there are approximately 50 targets close to the 1-d alias curves. The comparison with Kepler surveys shows that f_{match} is typically well below half. It is possible that the slightly better agreement with M13 ($f_{match} = 0.42$) compared to A18 and S19/S21 ($\sim 0.2 - 0.25$) is simply that the former sample comprises of Kepler objects of interest that, on average, rotate slower than the full Kepler field sample in M13, and the latter sample was pre-vetted to contain main-sequence targets (which are more likely to have longer P_{rot}). Finally, the two ground-based surveys, N16 (MEarth) and L22 (ZTF) have better matches, with f_{match} values of 0.58 and 0.82, respectively. Interestingly, whilst there appear to be no targets with 1-day aliases in N16, a notable number have literature P_{rot} close to 1-day. On the other hand, the L22 panel indicates several dozens of targets that match closely to the 1-day alias harmonics. The good agreement in both of these might be because both surveys target early M-stars, that typically take longer to spin-down, but this may also be indicative of an effective approach to screen out poor quality data from TESSILATOR lightcurves.

5 CONCLUSIONS

We present our new TESSILATOR code, which is available online. Whilst other software tools exist for working with TESS data, TESSILATOR is unique because it provides an all-in-one package for downloading image files, extracting aperture photometry, assessing

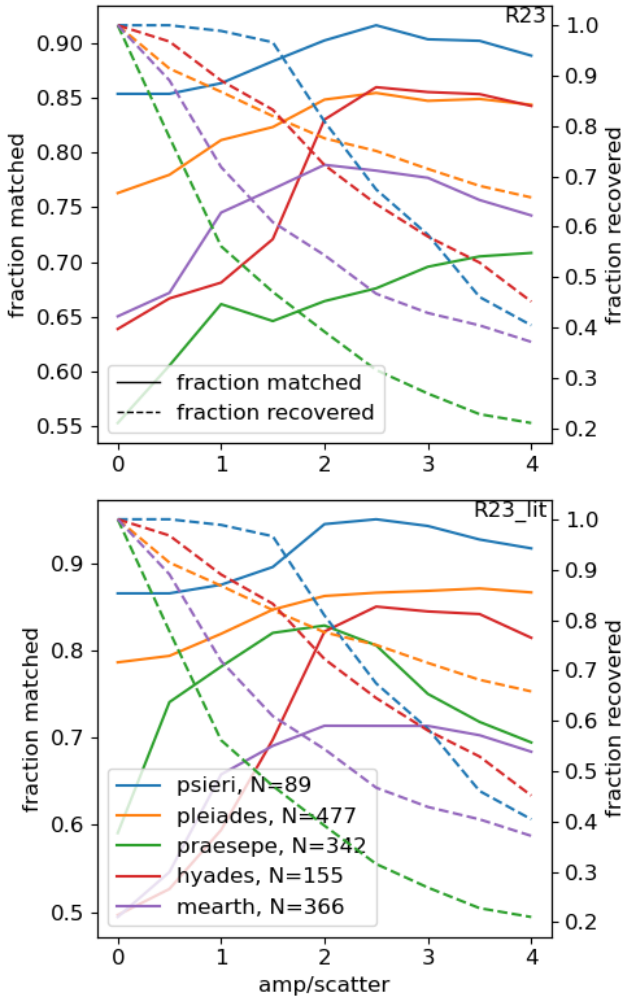


Figure 10. The relationships between both the period matching fraction (f_{grp} , solid lines) and fraction of recovered targets (f_{rec} , dashed lines) as a function of AS. The top and bottom panels represent the results for the R23 and R23_lit samples, respectively. The numbers in the legend represent the total number of targets in each group when AS=0.

the background contamination, processing lightcurves, performing LSP analyses and calculating P_{rot} . The code requires minimal input from the user and can be executed with simple command-line prompts. In this paper, we describe all our methods in a conceptual way, providing examples from real data to guide the narrative. We tested our code by comparing our TESSILATOR periods for a sample of 1560 stars comprising of members of 4 young groups and a field-star sample, with periods measured from two independent sources. The results indicate very good (65-90 per cent) agreement across all groups, which validates TESSILATOR as a reliable method for measuring P_{rot} . We also compare our software with several large field star surveys, finding reasonable agreement for TESS-based samples, as well as survey with longer observing baselines, when the P_{rot} is within the observing capabilities of TESS. Unsurprisingly, for targets with $P_{\text{rot}} > 13$ d, TESSILATOR is generally unable to find a matching value.

With the period validation successfully implemented, we believe that TESSILATOR can now be used for a large number of scien-

tific applications. To name a few, these include: understanding the evolution of P_{rot} and angular momentum by observing targets in young open clusters; testing new empirical models of Gyrochronology; investigating the connection between age, rotation and activity (or other parameters that vary with age/rotation); and identifying fast rotators as potentially young stars in large-scale surveys. Regarding this final application, TESSILATOR has already been used as part of the target selection strategy for a 5-year spectroscopic observing campaign to identify nearby, young stars using the 4-metre Multi-Object Spectroscopic Telescope (MOST). From an initial sample of $\sim 1.1 \times 10^6$ G/K-type stars within 500 pc, TESSILATOR identified $\sim 20,000$ fast rotators (and therefore young star candidates) which are scheduled for observation as part of the 4MOST Survey of Young Stars (4SYS).

Future TESSILATOR releases are anticipated, which will be largely driven by feedback from users. In our next version of the code, we aim to implement data-driven methods to improve reliability of measurements, which will lead to better ways to quantify the quality indicators. We hope the community find the tool a useful, unique addition to the large suite of software already available for use, and we are planning to use TESSILATOR for several scientific applications in the near future.

ACKNOWLEDGEMENTS

We are indebted to an anonymous referee, who provided constructive and thoughtful comments that led to a significant improvement in the manuscript. A.S. Binks acknowledges financial support from the Eberhard Karls Universität Tübingen and from the Massachusetts Institute of Technology. H.M. Günther was supported by the National Aeronautics and Space Administration through Chandra Award Number AR3-24001X issued by the Chandra X-ray Center, which is operated by the Smithsonian Astrophysical Observatory for and on behalf of the National Aeronautics Space Administration under contract NAS8-03060. This paper includes data collected from the TESS mission, obtained from the MAST data archive at the Space Telescope Science Institute (STScI). This work has made use of data from the European Space Agency (ESA) mission Gaia (<https://www.cosmos.esa.int/gaia>), processed by the Gaia Data Processing and Analysis Consortium (DPAC, <https://www.cosmos.esa.int/web/gaia/dpac/consortium>). Funding for the DPAC has been provided by national institutions, in particular the institutions participating in the Gaia Multilateral Agreement. The authors acknowledge support by the High Performance and Cloud Computing Group at the Zentrum für Datenverarbeitung of the University of Tübingen, the state of Baden-Württemberg through bwHPC and the German Research Foundation (DFG) through grant no INST 37/935-1 FUGG.

DATA AVAILABILITY

TESSILATOR is a publicly-available code, which is currently hosted at the following Git-Hub link: <https://github.com/alexibinks/teossilator>. The code operates under an MIT-style license. The full version of Table 3 is available in electronic format, and we plan to make the data accessible with the VizieR catalog service, provided by Centre de données astronomiques de Strasbourg. The data used to construct Figure 13 is available upon request.

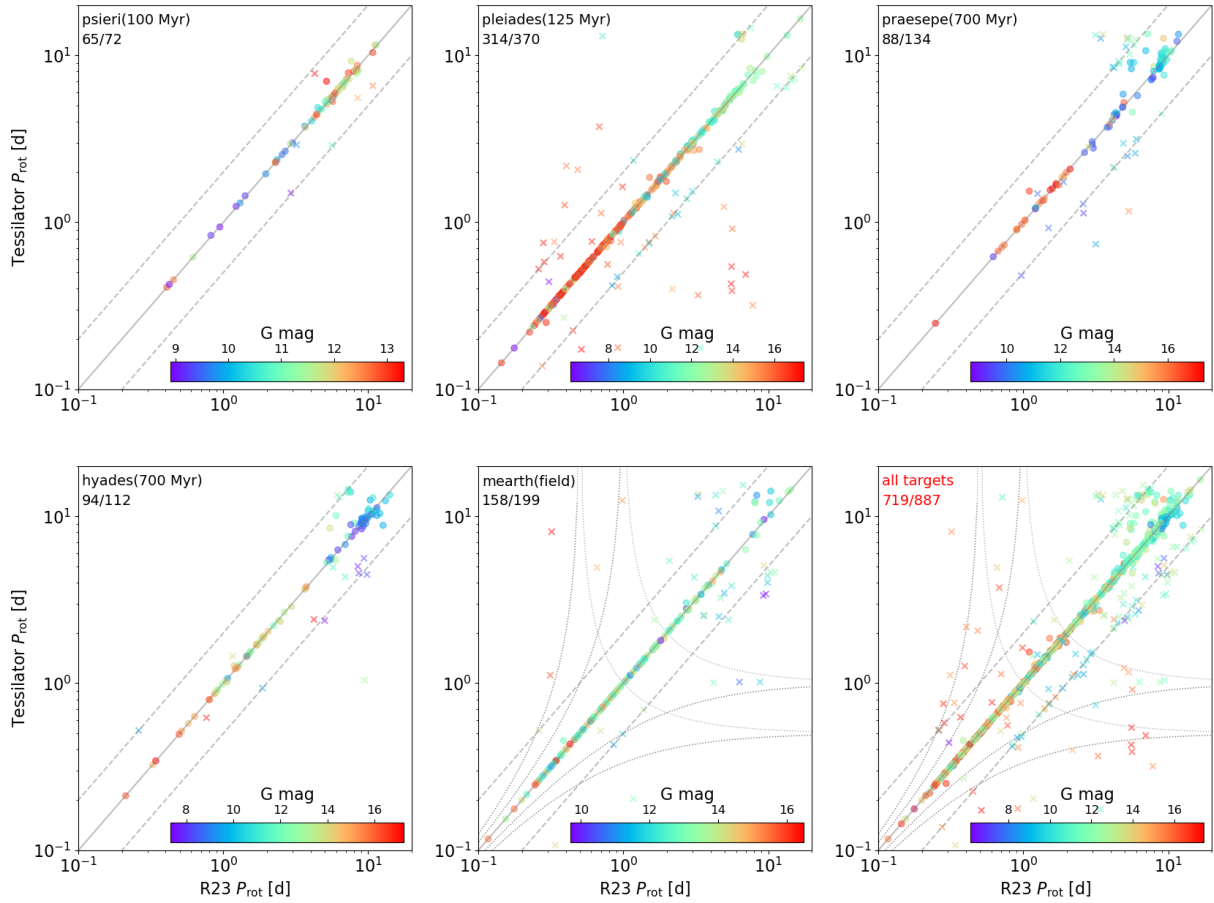


Figure 11. A comparison of P_{rot} values between TESSILATOR and R23 for the 5 separate groups and the combined sample (bottom-right), in the case where the fixed criteria are applied and $AS=2$. Filled circles and crosses are the targets that either satisfy, or do not satisfy the period matching criteria, respectively. The numerator and denominator in the fractions shown in the top-left of each panel represent the number of period matches and the number of targets available for testing. Symbols are colour-coded by their Gaia G magnitude and grey lines represent cases where there is equivalence, 1:2, and 2:1. The curved, dashed lines represent the 1-day alias failure modes, using equation 47 in VanderPlas (2018), with $n = 0, \pm 1$ and ± 2 .

REFERENCES

- Aigrain S., Foreman-Mackey D., 2023, *ARA&A*, **61**, 329
- Aigrain S., Parviainen H., Roberts S., Reece S., Evans T., 2017, *MNRAS*, **471**, 759
- Amard L., Palacios A., Charbonnel C., Gallet F., Georgy C., Lagarde N., Siess L., 2019, *A&A*, **631**, A77
- Angus R., Aigrain S., Foreman-Mackey D., McQuillan A., 2015, *MNRAS*, **450**, 1787
- Angus R., Morton T., Aigrain S., Foreman-Mackey D., Rajpaul V., 2018, *MNRAS*, **474**, 2094
- Angus R., et al., 2019, *AJ*, **158**, 173
- Astropy Collaboration et al., 2022, *ApJ*, **935**, 167
- Auvergne M., et al., 2009, *A&A*, **506**, A11
- Bakos G. Á., Lázár J., Papp I., Sári P., Green E. M., 2002, *PASP*, **114**, 974
- Baluev R. V., 2008, *MNRAS*, **385**, 1279
- Barnes S. A., 2003, *ApJ*, **586**, 464
- Barnes S. A., 2007, *ApJ*, **669**, 1167
- Basri G., 2021, An Introduction to Stellar Magnetic Activity, doi:10.1088/2514-3433/ac2956.
- Basri G., Nguyen H. T., 2018, *ApJ*, **863**, 190
- Bell C. P. M., Mamajek E. E., Naylor T., 2015, *MNRAS*, **454**, 593
- Binks A. S., Jeffries R. D., Maxted P. F. L., 2015, *MNRAS*, **452**, 173
- Binks A. S., et al., 2022, *MNRAS*, **513**, 5727
- Biser I., Millman G., 1965, Tables of Offset Circle Probabilities for a Normal Bivariate Elliptical Distribution. Technical report ECQM-2625, U.S. Army Electronics Command, <https://books.google.co.uk/books?id=5XBGAAAAAYAAJ>
- Borucki W. J., 2016, *Reports on Progress in Physics*, **79**, 036901
- Bouvier J., 2007, in Bouvier J., Appenzeller I., eds, IAU Symposium Vol. 243, IAU Symposium. pp 231–240 (arXiv:0712.2988), doi:10.1017/S1743921307009593
- Bradley L., et al., 2022, astropy/photutils: 1.5.0, doi:10.5281/zenodo.6825092, <https://doi.org/10.5281/zenodo.6825092>
- Brasseur C. E., Phillip C., Fleming S. W., Mullally S. E., White R. L., 2019, Astrocut: Tools for creating cutouts of TESS images (ascl:1905.007)
- Brun A. S., Browning M. K., 2017, *Living Reviews in Solar Physics*, **14**, 4
- Burke C. J., et al., 2020, TESS-Point: High precision TESS pointing tool, Astrophysics Source Code Library (ascl:2003.001)
- Caldwell D. A., et al., 2020, *Research Notes of the American Astronomical Society*, **4**, 201
- Carrington R. C., 1863, Observations of the spots on the Sun: from November 9, 1853, to March 24, 1861, made at Redhill
- Carter J. A., Winn J. N., 2009, *ApJ*, **704**, 51
- Ceillier T., et al., 2017, *A&A*, **605**, A111
- Clayton Z. R., van Saders J. L., Llama J., Sadowski P., Quach B., Avallone E. A., 2022, *ApJ*, **927**, 219
- Clayton Z. R., van Saders J. L., Cao L., Pinsonneault M. H., Teske J., Beaton R. L., 2024, *ApJ*, **962**, 47
- Colman I. L., Angus R., David T., Curtis J., Hattori S., Lu Y. L., 2024, arXiv e-prints, p. arXiv:2402.14954

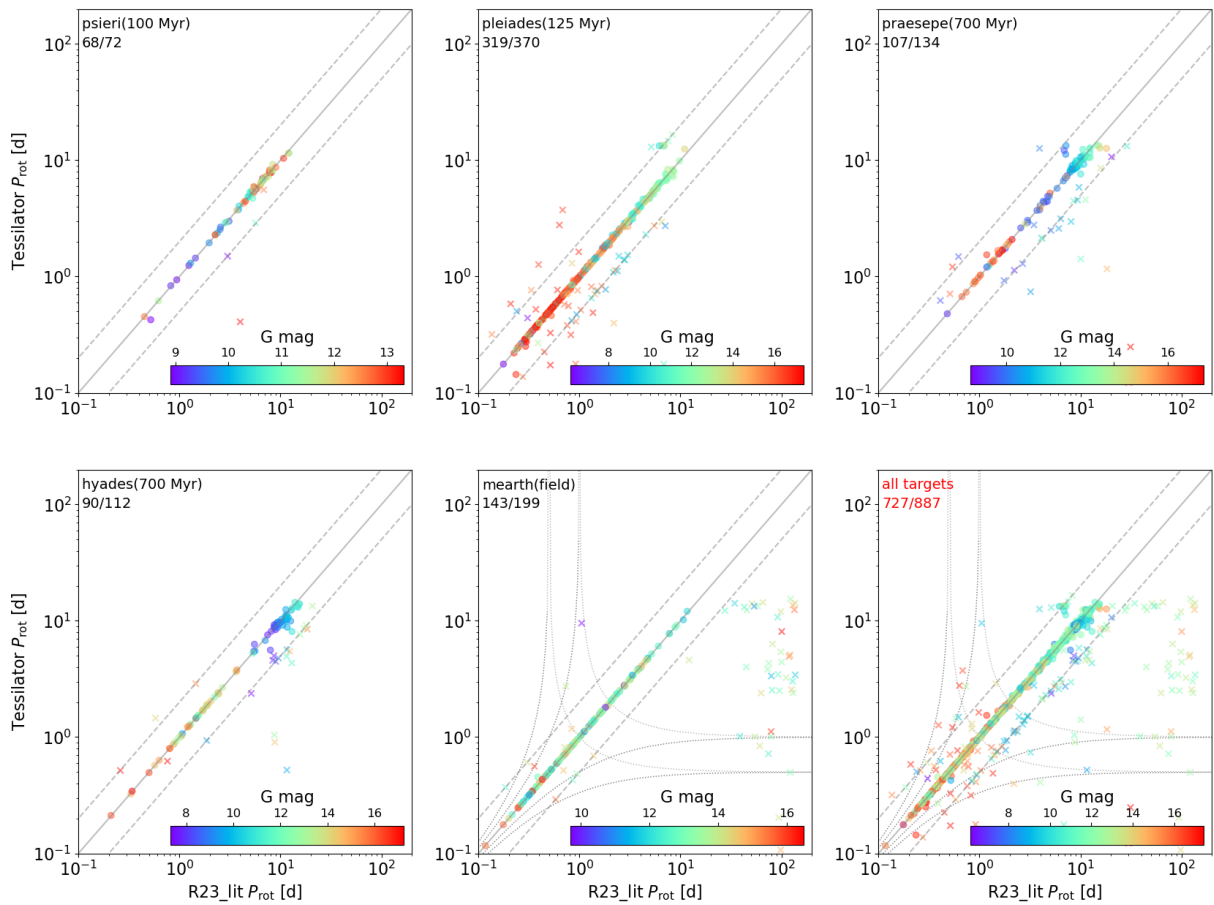


Figure 12. The same as Figure 11, this time with the R23_lit sample for comparison.

Curtis J. L., Agüeros M. A., Mamajek E. E., Wright J. T., Cummings J. D., 2019, *AJ*, **158**, 77

Davenport J. R. A., 2016, *ApJ*, **829**, 23

De Medeiros J. R., Alves S., Udry S., Andersen J., Nordström B., Mayor M., 2014, *A&A*, **561**, A126

Fausnaugh M. M., et al., 2021, *ApJ*, **908**, 51

Feinstein A. D., et al., 2019, *PASP*, **131**, 094502

Gaia Collaboration et al., 2023, *A&A*, **674**, A1

Gallet F., Bouvier J., 2013, *A&A*, **556**, A36

García R. A., et al., 2014, *A&A*, **572**, A34

Garraffo C., et al., 2018, *ApJ*, **862**, 90

Glebocki R., Gnacinski P., Stawikowski A., 2000, *Acta Astron.*, **50**, 509

Gorti U., Hollenbach D., 2009, *ApJ*, **690**, 1539

Guerrero N. M., et al., 2021, *ApJS*, **254**, 39

Günther M. N., et al., 2020, *AJ*, **159**, 60

Hattori S., Foreman-Mackey D., Hogg D. W., Montet B. T., Angus R., Pritchard T. A., Curtis J. L., Schölkopf B., 2022, *AJ*, **163**, 284

Hedges C., Angus R., Barentsen G., Saunders N., Montet B. T., Gully-Santiago M., 2020, *Research Notes of the American Astronomical Society*, **4**, 220

Holcomb R. J., Robertson P., Hartigan P., Oelkers R. J., Robinson C., 2022, *ApJ*, **936**, 138

Howell S. B., et al., 2014, *PASP*, **126**, 398

Irwin J., Hodgkin S., Aigrain S., Hebb L., Bouvier J., Clarke C., Moraux E., Bramich D. M., 2007, *MNRAS*, **377**, 741

Irwin J., Hodgkin S., Aigrain S., Bouvier J., Hebb L., Irwin M., Moraux E., 2008, *MNRAS*, **384**, 675

Jeffries R. D., Jackson R. J., Sun Q., Deliyannis C. P., 2021, *MNRAS*, **500**, 1158

Jenkins J. M., et al., 2016, in Chiozzi G., Guzman J. C., eds, *Society of*

Photo-Optical Instrumentation Engineers (SPIE) Conference Series Vol. 9913, *Software and Cyberinfrastructure for Astronomy IV*. p. 99133E, doi:10.1117/12.2233418

Kawaler S. D., 1988, *ApJ*, **333**, 236

Koenigl A., 1991, *ApJ*, **370**, L39

Kraft R. P., 1967, *ApJ*, **150**, 551

Kunimoto M., Winn J., Ricker G. R., Vanderspek R. K., 2022, *AJ*, **163**, 290

Lightcurve Collaboration et al., 2018, *Lightcurve: Kepler and TESS time series analysis in Python*, *Astrophysics Source Code Library*, record ascl:1812.013 (ascl:1812.013)

Lin C.-L., Ip W.-H., Hsiao Y., Chang T.-H., Song Y.-h., Luo A. L., 2023, *AJ*, **166**, 82

Linsky J. L., Hunten D. M., Sowell R., Glackin D. L., Kelch W. L., 1979, *ApJS*, **41**, 481

Lomb N. R., 1976, *Ap&SS*, **39**, 447

Lu Y. L., Curtis J. L., Angus R., David T. J., Hattori S., 2022, *AJ*, **164**, 251

Mamajek E. E., Hillenbrand L. A., 2008, *ApJ*, **687**, 1264

McQuillan A., Aigrain S., Mazeh T., 2013, *MNRAS*, **432**, 1203

Naylor T., 1998, *MNRAS*, **296**, 339

Newton E. R., Irwin J., Charbonneau D., Berta-Thompson Z. K., Dittmann J. A., West A. A., 2016, *ApJ*, **821**, 93

Noyes R. W., Hartmann L. W., Baliunas S. L., Duncan D. K., Vaughan A. H., 1984, *ApJ*, **279**, 763

Oelkers R. J., et al., 2018, *AJ*, **155**, 39

Owen J. E., Ercolano B., Clarke C. J., 2011, *MNRAS*, **412**, 13

Pallavicini R., Golub L., Rosner R., Vaiana G. S., Ayres T., Linsky J. L., 1981, *ApJ*, **248**, 279

Picogna G., Ercolano B., Owen J. E., Weber M. L., 2019, *MNRAS*, **487**, 691

Pollacco D. L., et al., 2006, *PASP*, **118**, 1407

Poore E., Carini M., Dingler R., Wehrle A. E., Wiita P. J., 2024, *ApJ*, **966**,

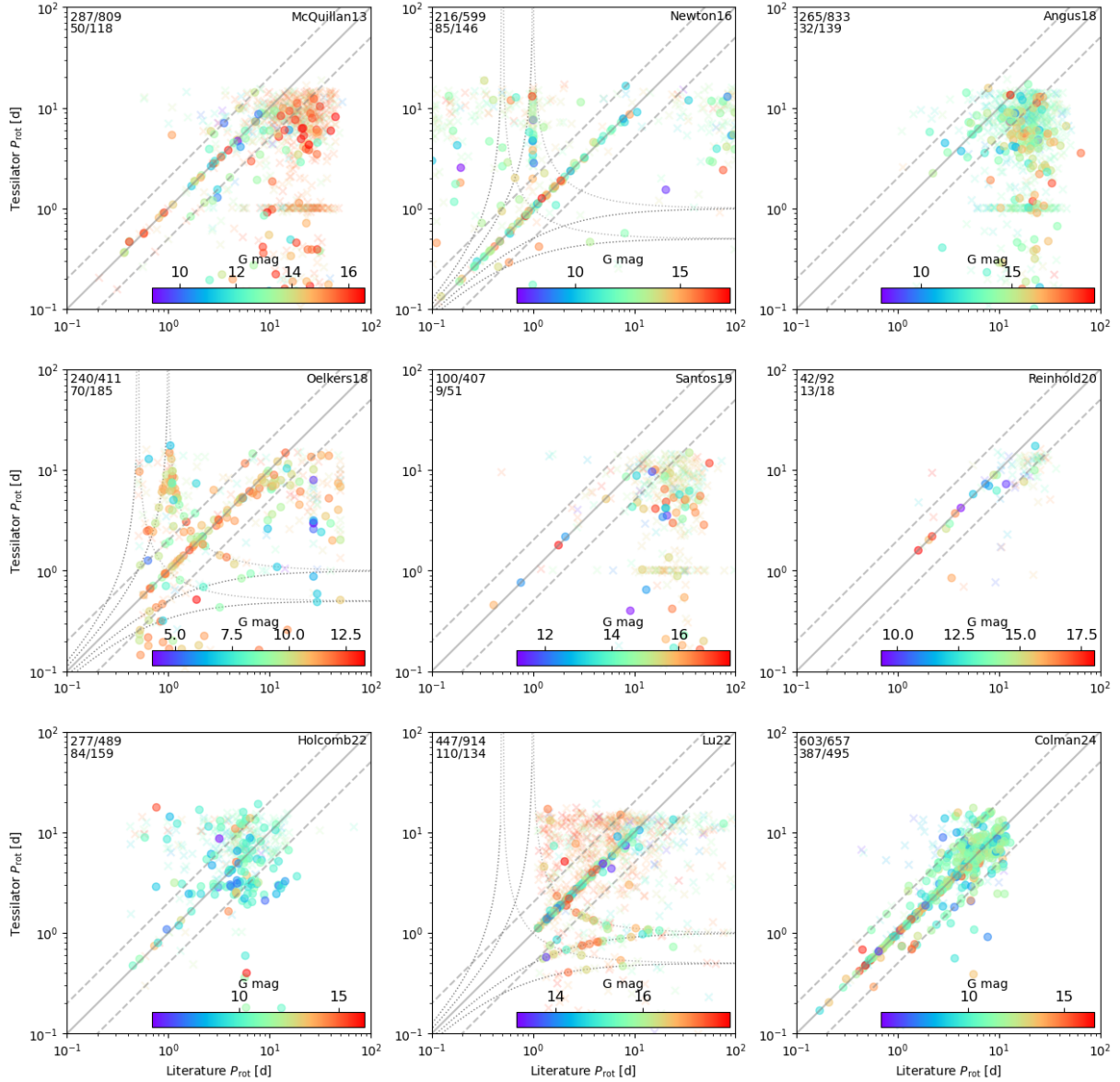


Figure 13. Comparison of P_{rot} between TESSILATOR and 10 field-star surveys. Crosses and circles indicate targets that fail and pass the quality criteria (given in §4.1), respectively, where the fractions in the top-left corners of each panel indicate the ratio of P_{rot} values that are in agreement. Targets are colour-coded by the range of G magnitudes across both the fail/pass sub-samples. Note that we combine the S19 and S21 sample into one panel.

158

Raetz S., Stelzer B., Damasso M., Scholz A., 2020, *A&A*, **637**, A22
 Rampalli R., Smock A., Newton E. R., Daniel K. J., Curtis J. L., 2023, *ApJ*, **958**, 76
 Ramsay G., Doyle J. G., Doyle L., 2020, *MNRAS*, **497**, 2320
 Reinhold T., Hekker S., 2020, *A&A*, **635**, A43
 Ricker G. R., et al., 2015, *Journal of Astronomical Telescopes, Instruments, and Systems*, **1**, 014003
 Riello M., et al., 2021, *A&A*, **649**, A3
 Santos A. R. G., García R. A., Mathur S., Bugnet L., van Saders J. L., Metcalfe T. S., Simonian G. V. A., Pinsonneault M. H., 2019, *ApJS*, **244**, 21
 Santos A. R. G., Breton S. N., Mathur S., García R. A., 2021, *ApJS*, **255**, 17
 Scargle J. D., 1982, *ApJ*, **263**, 835
 Schatzman E., 1962, *Annales d'Astrophysique*, **25**, 18
 Serna J., et al., 2021, *ApJ*, **923**, 177
 Skumanich A., 1972, *ApJ*, **171**, 565
 Soderblom D. R., Pilachowski C. A., Fedele S. B., Jones B. F., 1993, *AJ*, **105**,

2299

Spada F., Lanzafame A. C., 2020, *A&A*, **636**, A76
 Suárez Mascareño A., et al., 2018, *A&A*, **612**, A89
 Toledo-Padrón B., et al., 2019, *MNRAS*, **488**, 5145
 VanderPlas J. T., 2018, *ApJS*, **236**, 16
 Vanderspek R., Doty J., Fausnaugh M., 2018, *TESS Instrument Handbook*, Tech., Kavli Institute for Astrophysics and Space Science, Massachusetts Institute of Technology
 Watson C. L., Henden A. A., Price A., 2006, *Society for Astronomical Sciences Annual Symposium*, **25**, 47
 Wilson O. C., 1978, *ApJ*, **226**, 379
 Zahn J. P., 1992, *A&A*, **265**, 115
 Zechmeister M., Kürster M., 2009, *A&A*, **496**, 577
 van Saders J. L., Ceillier T., Metcalfe T. S., Silva Aguirre V., Pinsonneault M. H., García R. A., Mathur S., Davies G. R., 2016, *Nature*, **529**, 181

APPENDIX A: CBV TESTS USED FOR SELECTING LIGHTCURVES

In §3.2.2 we describe that there are two separate tests (CBV test 1 and CBV test 2) used to determine whether a CBV-corrected lightcurve should be selected from which to calculate P_{rot} . Each test uses a scoring system, where the CBV-corrected lightcurve must score higher than the original lightcurve (a draw results in the original lightcurve being selected). For CBV test 1, the fluxes from each lightcurve are first normalised using the median flux value (f_{med}). We shall label these normalised fluxes as f_{norm} . For CBV test 1, we have the following rounds:

(1a) **Which lightcurve has the least extreme outliers?**

The normal-adjusted MAD flux value from f_{norm} is calculated (labelled f_{MAD}), and the lightcurve with the least number of f_{norm} values outside the range $f_{\text{med}} \pm f_{\text{MAD}}$ is awarded the point.

(1b) **Which lightcurve has the lowest f_{MAD} value?**

The lightcurve with the lowest f_{MAD} value wins the point.

(1c) **Which lightcurve is best matched to a sinusoidal fit?**

A sinusoidal fit of the form $f_{\text{norm}} = f_0 + A \sin\left(\frac{2\pi}{P_{\text{rot}}}t + \phi\right)$ is used, where f_0 is a constant, A is the amplitude, P_{rot} is the period, ϕ is the phase and t is the time coordinate to be fitted. The lightcurve that provides the lowest reduced χ^2 score wins the point.

For CBV test 2, we use features from the periodogram analysis to assess which lightcurve gives the best results. The lightcurves used here have been passed through all the processing steps. There are 5 parts to this test, which are as follows:

(2a) **Straight line or sinusoidal fit?**

Using the AIC procedure described in §3.3.4, determine whether the best fit corresponds to a straight line or a sinusoid. If the latter, then a point is scored.

(2b) **How smooth are the lightcurves?**

If the “jump flag” (described in §3.5) returns a value of 1, a point is scored.

(2c) **False Alarm Probabilities**

Measure the ratio between the highest LSP power output and False Alarm Probability corresponding to a 1 per cent threshold. Whichever lightcurve has the highest value wins the point.

(2d) **The amplitude-to-scatter ratio**

The ratio of the amplitude and the typical scatter of the phase-folded lightcurve (described in §3.4.4) is calculated for both lightcurves. The highest value wins the point.

(2e) **Total number of data points**

The lightcurve with the largest number of data points wins the point.

This paper has been typeset from a $\text{\TeX}/\text{\LaTeX}$ file prepared by the author.